DEPARTMENT OF PHYSICS, UNIVERSITY OF JYVÄSKYLÄ
RESEARCH REPORT No. 7/1983

A 4π γ-RAY MULTIDETECTOR SYSTEM FOR HEAVY-ION PHYSICS; POPULATION AND DECAY OF HIGH SPIN STATES IN $^{157\text{-}161}$Yb

BY
MARKKU JÄÄSKELÄINEN

Academic dissertation
for the Degree of
Doctor of Philosophy

Jyväskylä, Finland
May 1983

URN:ISBN:978-951-39-9483-9
ISBN 978-951-39-9483-9 (PDF)
ISSN 0075-465X

Jyväskylän yliopisto, 2023

ISBN 951-678-900-5
ISSN 0075-465X

DEPARTMENT OF PHYSICS, UNIVERSITY OF JYVÄSKYLÄ
RESEARCH REPORT No. 7/1983

A 4π γ-RAY MULTIDETECTOR SYSTEM FOR HEAVY-ION PHYSICS; POPULATION AND DECAY OF HIGH SPIN STATES IN $^{157-161}$Yb

BY
MARKKU JÄÄSKELÄINEN

Academic dissertation
for the Degree of
Doctor of Philosophy

To be presented, by permission of the
Faculty of Mathematics and Natural Sciences
of the University of Jyväskylä,
for public examination in Auditorium S-212 of the
University on May 30, 1983, at 12 o'clock noon.

Jyväskylä, Finland
May 1983

PREFACE

The work presented in this thesis has been carried out during the years 1979 - 1982 at the Washington University (St.Louis, Missouri, USA), in the Oak Ridge National Laboratory (Oak Ridge, Tennessee, USA) and at the University of Jyväskylä. I wish to express my sincere thanks to all these institutes for providing the excellent working conditions.

I am particularly indebted to Professor D.G. Sarantites and Dr. J.R. Beene, who offered a wealth of ideas during the work. I am also grateful to Professor J. Hattula. His continuous interest and encouragement in my studies and research work has been of great value. I want to express my gratitude to all my co-workers. Especially I would like to thank Dr. F.A. Dilmanian, Dr. M.L. Halbert and Dr. D.C. Hensley.

I am obliged to Miss T. Tuominen, who carefully typed this thesis.

Above all I dedicate warmest thanks to my wife, Raili, not only for her encouragement but also for conserable help in programing the data analysis and calibration methods.

For financial support I am indepted to the Washington University and the University of Jyväskylä. This work was also supported by a grant from Emil Aaltonen Foundation and by travel grants from the Finnish Cultural Foundation and the Academy of Finland, for which I wish to express my gratitude.

Jyväskylä, April 1983

Markku Jääskeläinen

A 4π γ - RAY MULTIDETECTOR SYSTEM FOR HEAVY-ION PHYSICS;
POPULATION AND DECAY OF HIGH SPIN STATES IN $^{157-161}$Yb

Abstract

Construction of a new type of spectrometer for the investigation of nuclear structure at high angular momentum and of the mechanisms of heavy-ion induced reactions is reported. The spectrometer consists of 72 NaI(Tl) detectors packed in a 4π arrangement. With this instrument the γ-ray multiplicity, the total γ-ray energy, the angular correlations of emitted γ-rays, and the time relationships between the γ-rays in a cascade can be obtained for each event. The pulse height spectra of the γ-rays associated with these parameters can also be obtained. The geometric arrangement and the associated electronics and data aquisition system are discussed. The calibrations and data analysis methods for obtaining the entry state populations and for obtaining the associated γ-ray energy spectra are discussed. Unique studies of the role of the angular momentum in heavy-ion fusion reactions and the structure of transitional rare earth nuclei are reported.

The statistical model calculations reproduce the main features of the observed entry state populations in heavy-ion fusion reactions. From the observed γ-ray multiplicity distributions the entrance channel orbital angular momentum distribution leading to fusion has been deduced. A new decay mode involving localized dipole radiction at half the accompanying stretched E2 radiation is found in $^{157-161}$Yb at high spin. The appearance of this decay mode correlates smoothly with neutron number. In addition a region of noncollective behaviour of ^{157}Yb and ^{158}Yb at intermediate spins is observed. Possible interpretations are presented in terms of the evolution of the nuclear shapes from prolate to aligned-quasiparticle oblate to collective oblate nucleus.

Contents

1. INTRODUCTION

The behavior of nuclei at large angular momentum is one of the most fascinating aspects of nuclear physics to be opened up via increasing opportunities to produce and study high spin states. The experimental methods for producing nuclei at high spin have developed rapidly. Using radioactive β- and α-decay evidence for shell-model isomers [1] and rotational structure [2] was derived in the early 50's. The rotational states were further studied using Coulomb excitation and large enhancement in electric quadrupole transition probabilities was observed [3]. The fusion reactions with light ions were used to populate the nuclei up to spin $\sim$ 25 $\hbar$ in the early 60's [4] and the heavy-ion fusion reactions became a prime tool for producing nuclei at high angular momentum in the late 60's [5]. Since then, the study of the nature and the behavior of heavy-ion fusion reactions has been of great interest. The questions of the angular momentum and excitation energy dependence are the most interesting ones.

With heavy-ions it is possible to produce all the angular momentum a nucleus can hold. Thus the heavy-ion fusion reactions are extremely useful tools in nuclear high-spin spectroscopy and the main task is to identify proper signals from nuclei at high angular momentum. Using heavy-ion fusion reactions the discrete line-spectroscopy has been "pushed up" with the aid of different selective spectroscopic devices. The known discrete lines have been studied up to I $\sim$ 40 $\hbar$ [6,7] in some nuclei but the average "flag" is still at I $\sim$ 30 $\hbar$. Also other experimental methods have been developed to extract information from unresolved γ-ray spectra. Multidetector arrays were used first and, more recently, good-efficiency γ-ray coincidence-sum spectrometers and $\gamma\gamma$-energy correlation techniques

have been employed.

The structure of the rare earth nuclei with neutron number $N \sim 90$ has been investigated and discussed most intensively. The well established rotational behavior of nuclei with $N > 92$ [8] and single-particle structure of nuclei with $N \lesssim 85$ [6] has brought the focus to the transitional nuclei at $N \sim 85 - 90$. The theoretical discussion has introduced a possibility for a shape change of transitional nuclei with increasing angular momentum [9,10]. Thus these nuclei in the border of a deformation region play an important role in understanding the behavior of the spinning quantized nucleus [9].

In the first part of this thesis a description of a new type of spectrometer, a 4π multidetector system, for the investigation of heavy-ion reactions and nuclear structure at high spin is done. In Chapter 2 the basic concepts of the spectrometer are described in detail and in Chapter 3 the experimental methods of the first experiments done with ^{20}Ne induced reactions on ^{144}Nd and ^{146}Nd are described. The results from these experiments are discussed in the second part of this thesis. The population of the entry states in heavy-ion fusion reactions is discussed in Chapter 4 and the decay of the entry states in $^{157-161}Yb$ is discussed in Chapter 5. Finally the evolution of the nuclear structure as a function of spin and neutron number in the transitional rare earth nuclei is discussed in Chapter 6. The thesis is mainly based on the data published in the following articles:

1. D.G. Sarantites, M. Jääskeläinen, J.T. Hood, R. Woodward, J.H. Barker, D.C. Hensley, M.L. Halbert and Y.D. Chan, J. de Phys. C 10 (1980) 269
   https://doi.org/10.1051/jphyscol:19801030

2. M. Jääskeläinen, D.G. Sarantites, R. Woodward, F.A. Dilmanian, J.T. Hood, R. Jääskeläinen, D.C. Hensley, M.L. Halbert and
   J.H. Barker,
   Nucl. Instr. Meth. 204 (1983) 385
   https://doi.org/10.1016/0167-5087(83)90068-6

3. D.G. Sarantites, M. Jääskeläinen, R. Woodward, F.A. Dilmanian, D.C. Hensley, J.H. Barker, J.R. Beene, M.L. Halbert and W.T. Milner,
Phys. Lett. 115 B (1982) 441
https://doi.org/10.1016/0370-2693(82)90388-4

4. M. Jääskeläinen, D.G. Sarantites, R. Woodward, F.A. Dilmanian, H. Puchta, J.R. Beene, J. Hattula, M.L. Halbert, D.C. Hensley and J.H. Barker,
Phys. Rev. Lett. 49 (1982) 1387
https://doi.org/10.1103/PhysRevLett.49.1387

5. M. Jääskeläinen, D.G. Sarantites, F.A. Dilmanian, R. Woodward, H. Puchta, J.R. Beene, J. Hattula, M.L. Halbert and D.C. Hensley,
Phys. Lett. 119 B (1982) 65
https://doi.org/10.1016/0370-2693(82)90244-1

6. M. Jääskeläinen, D.G. Sarantites, F.A. Dilmanian, R. Woodward, H. Puchta, J.R. Beene, J. Hattula, M.L. Halbert, D.C. Hensley and J.H. Barker
Nucl. Phys. A 396 (1983) 319c
https://doi.org/10.1016/0375-9474(83)90028-3

7. M. Jääskeläinen, D.G. Sarantites, F.A. Dilmanian, R. Woodward, H. Puchta, J.R. Beene, J. Hattula, M.L. Halbert and D.C. Hensley,
Phys. Scripta (in press)
https://doi.org/10.1088/0031-8949/1983/T5/033

2. SPIN SPECTROMETER - A 4π MULTIDETECTOR SYSTEM

Detection of the electromagnetic radiation emitted in heavy-ion induced reactions provides a good tool for the investigation of both nuclear structure at very high angular momentum and reaction mechanisms. In such investigations, experiments are becoming increasingly complex because high γ-ray multiplicities are usually involved in heavy-ion reactions.

Measurements of the γ-ray multiplicity (M) have been made by utilizing high-order coincidence techniques [11-19]. With the application of up to fourteen NaI detectors useful information about the angular momentum transfer in heavy-ion reactions has been obtained [20] and new evidence about non-equilibrium effects in such reactions has been deduced [21,22]. So far multiplicity experiments have been done with relatively small detectors sampling a small total solid angle. This method provides information about the multiplicity distribution from a large number of events, giving only estimates of the first few moments of the M distribution. The higher moments of the M distribution are in practice difficult to determine accurately. No precise measurements of the skewness (third moment) have been reported and for many interesting processes even the width (second moment) of the multiplicity distribution is difficult to obtain.

A second generation of experiments utilizes γ-ray coincidence-sum spectrometers for estimation of the total energy carried off by γ-rays [23,24]. This kind of spectrometer has been used to determine the entry line in heavy-ion induced reactions and as a tool for nuclear structure investigations. Although sum spectrometers provide a connection between the observed pulse height and total γ-ray energy on an event-by-event

basis, they give only a crude estimate of M and they suffer from three serious drawbacks: The small target-to-detector distance makes it very difficult to distinguish the pulses due to neutrons from those due to γ-rays, the total-energy efficiency of the sum spectrometers built thus far is typically 60 % and the correlated total energy and the associated multiplicity cannot be deduced simultaneously.

The above points emphasize the need for a new type of instrument capable of measuring simultaneously the γ-ray multiplicity and the total γ-ray energy. The main criteria for the design of this type of spectrometer are [25]: the number of the detector elements in the sphere should be at least twice the maximum multiplicity to be measured; the detector shell must subtend a solid angle of nearly 4π and be sufficiently thick for nearly complete absorption of the γ-rays involved; and the inner diameter of the shell should be large enough for adequate separation of γ-rays from neutrons by time of flight (TOF) and for accomodating a large reaction chamber, essential to a versatile instrument.

This kind of spectrometer can be used in a large variety of experiments and can provide unique information about the properties of nuclei at very high angular momentum and about the mechanisms of heavy-ion induced reactions. The experimental quantities that can be measured by such a device on an event-by-event basis are: the γ-ray coincidence fold and the associated total pulse height, the pulse heights of individual γ-ray transitions, the neutron multiplicity, the angular correlations among the γ-rays in the cascade, the spin direction of the initial state in the γ-cascade, and the time and energy correlations among the various groups of γ-rays in each cascade.

In this chapter the performance of such a spectrometer built at Washington University and installed at the Holifield Heavy-Ion Research

Facility (HHIRF) at Oak Ridge National Laboratory is reported. This spectrometer, known as the Spin Spectrometer, has been installed in a beam-line at the HHIRF, which provides heavy-ion beams from the Oak Ridge Isochronous Cyclotron (ORIC), the 25 MV Tandem Accelerator, or from coupled operation of the 25 MV Tandem injected into the ORIC.

The specific design and geometry of this apparatus are described in Sec. 2.1 and the performance of the individual detectors is given in Sec. 2.2. The electronics and data acquisition systems are discussed in Sec. 2.3. The methods of calibration of the spectrometer are described in Sec. 2.4. Finally, neutron identification and the response of the spectrometer to neutrons are discussed in Sec. 2.5.

2.1. Design and geometry

The spin spectrometer consists of an array of 72 closely packed NaI detectors approximating a hollow sphere with inner radius 178 mm and shell thickness 178 mm. Each detector is a tapered prism that can be removed radially. The cross section of twelve of the detectors is a regular pentagon. Each of the pentagonal detectors is surrounded by five identical detectors of irregular hexagonal cross section. The polyhedron formed by the front faces of the detectors is shown in fig. 1 where the twelve pentagonal surfaces are marked in black. The area of each pentagon is 1.016 times that of each hexagon in order to have the solid angles of all detectors equal. Each pentagonal detector is located directly opposite another pentagonal detector. One such pair has been removed from the spectrometer to accomodate the beam entry and exit pipes which are welded to the inner spherical reaction chamber.

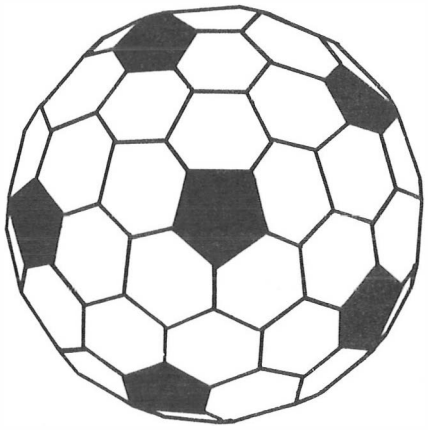

Fig. 1. Geometry of the Spin Spectrometer based on the truncated pentagonal hexecontahedron. The black areas represent the twelve regular pentagons.

The supporting frame, made of 2.54-cm dia. aluminium rods, is a dodecahedron consisting of twelve regular pentagons whose centers lie behind the centers of the pentagonal detectors. The frame is split into halves that stand on two independently movable platforms. The halves may be rolled back on tracks perpendicular to the beam line to give access to the reaction chamber. The tracks allow a maximum separation of 122 cm between the halves of the spectrometer. Fig. 2 shows the spectrometer standing on the platform.

The angular positions of the detectors in the spectrometer are listed in appendix 1. The effective solid angle of each NaI crystal is 1.344 % (96.8 % / 72) of 4 π. The 3.2 % loss is due to the wall thickness (1 mm) of the aluminium cans housing the NaI crystals and the internal light reflecting material (0.25 mm paper) inside the cans. There is no shielding between neighboring detectors.

Many kinds of nuclear events may occur under heavy-ion bombardment and the spectrometer has a very high efficiency for detecting radiation produced in any of them. Each experiment is therefore set up with auxiliary detectors to select the events of interest to a particular inves-

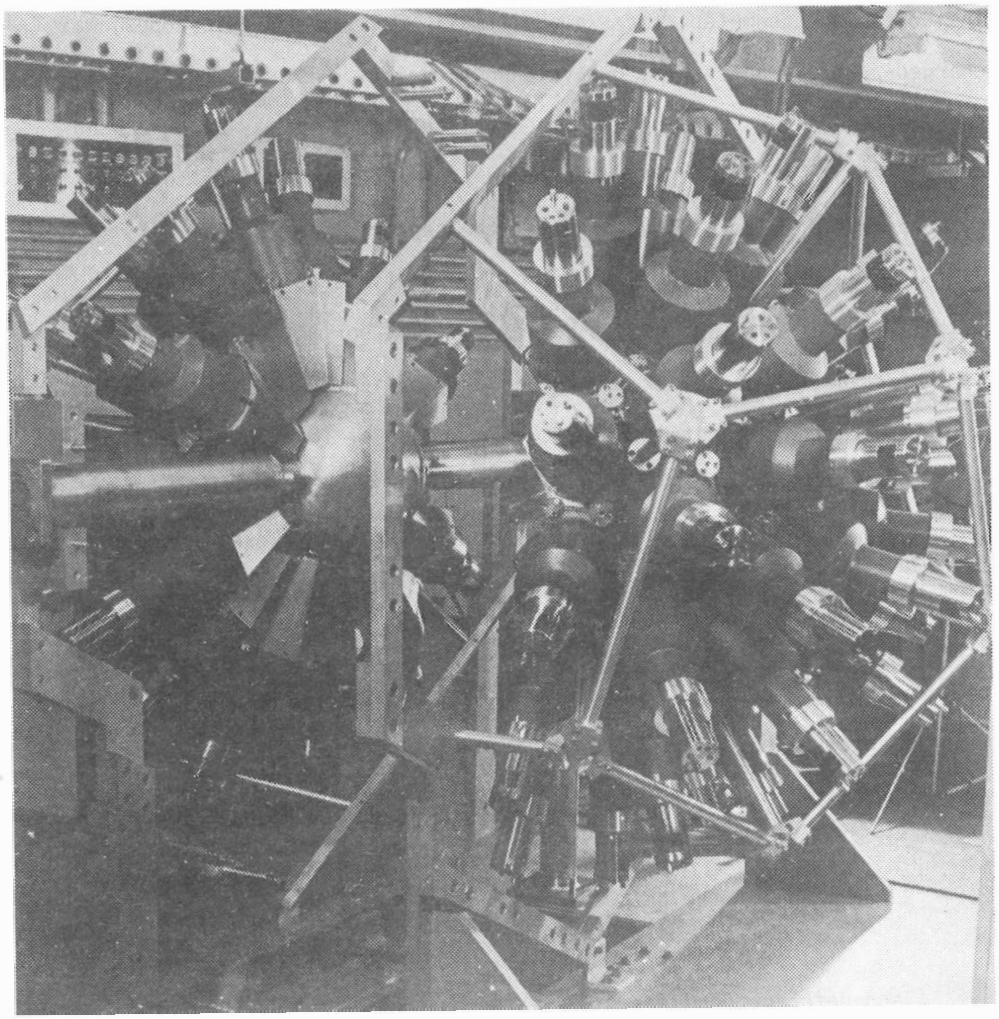

Fig. 2. Photograph of the Spin Spectrometer with one side fully open. Signal cables and exit pipe are not connected.

tigation, and data from the spectrometer for a given event are recorded only if a valid trigger has been supplied by the auxiliary system.

The reaction chamber permits various detector systems to be used inside the spectrometer, for example, small $\Delta E \times E$ silicon telescopes, NaI charged-particle detectors, or avalanche counters. External detectors such as Ge counters or neutron time-of-flight counters may also be used provided that NaI detectors are removed from the spectrometer to permit an unobstructed view of the target at the center of the sphere.

The reaction chamber consists of two hemispheres 3-mm thick with an inner diameter of 32 cm. It has four access ports, one of 6-cm diameter for the target holder and three of 8-cm diameter. The latter are coaxial with the NaI detectors at (θ, ϕ) angles of $(87.6^{o}, -102.6^{o})$, $(116.6^{o}, -72^{o})$ and $(138.6^{o}, 86.2^{o})$. Re-entrant covers for these ports are provided such that a Ge detector can be placed as close as 7.5 cm from the target. Any NaI detector in the spectrometer can be replaced by a Ge detector at a distance greater than 16.3 cm (the outer radius of the reaction chamber). The reaction chamber has been equipped with removable internal hardware for supporting particle detectors.

2.2. Performance of the NaI detectors

Each detector consists of Polyscin NaI(Tl) [26] coupled via a plano-concave glass window to an RCA 4522 photomultiplier tube. The voltage dividers in the tube base allow for adjustment of the potential of the focus grid in the phototube and the potential between the last dynode and the anode.

Linearity and counting-rate stability tests were made on several

detectors as a function of the tube-base adjustments. For linearity tests, a mixture of γ-ray sources with energies from 122 keV to 6130 keV was used. Higher energies were simulated by increasing the phototube voltage and attenuating the anode output so as to present the analysis system with the same pulse amplitudes. In this way the linearity was measured up to equivalent energies of $\sim$ 50 MeV. The counting-rate stability was measured with ^{60}Co sources of different strength.

The best counting rate stability with the present voltage dividers is achieved when the tube base controls are adjusted for nearly the maximum pulse-height output. With these settings, however, the phototubes are nonlinear for $E_\gamma \geq 3$ MeV. When this potentiometer is not at maximum the detectors give a linear response up to $\sim$ 50 MeV, but the counting-rate stability is poorer by a factor of three. Thus, depending on the application, the instrument can be optimized for linearity or stability. In the experiments described in this work the latter choice has been made and the pulse heights were corrected for the nonlinearity determined during the post-run calibrations with γ-ray sources. The counting-rate stability of a typical detector is illustrated in fig. 3 for a wide range of operating voltages. During the experiments the count-rate has been 8000 - 20000 c/s per detector and the operating voltage at $\sim$ 1900 V.

Neutrons are distinguished from γ-rays by their time of flight. The higher intensity and average velocity of neutrons at forward angles requires that the detectors with better timing performance are placed in forward positions. Before assembling the spectrometer, the timing performance of each detector was measured for ^{60}Co coincidences between the NaI and an NE-213 liquid scintillator. With the threshold set at 80 keV, the average fwhm for the NaI detectors was 2.1 ns and the average fwtm

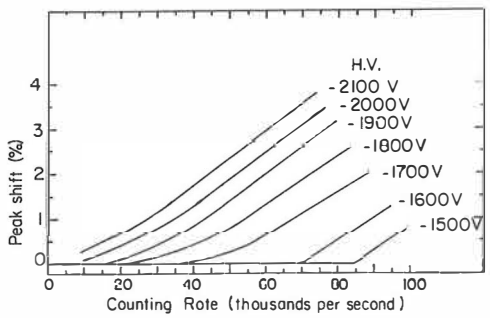

Fig. 3. Shift of the 1332-keV peak position as a function of counting rate, measured at various operating voltages for one detector element.

was 4.7 ns. The fwhm varied between 1.7 ns and 2.5 ns and the fwtm between 3.8 ns and 5.4 ns. For the detector placement actually adopted during assembly of the spectrometer, fig. 4b shows the time resolution averaged over each group of five detectors having the same θ. All detectors in the forward hemisphere have fwtm better than 4.7 ns. Reducing the high voltage by 100 volts increases the fwtm by about 0.2 ns, but higher voltages do not improve the timing performance significantly. The energy resolution of the NaI detectors varies between 7.7 % and 9.2 % for the 662 keV γ-ray from ^{137}Cs and between 5.6 % and 6.7 % for the 1332 keV γ-rays from ^{60}Co; the average values are 8.6 % and 6.3 % for the 662-keV and 1332 keV lines, respectively. The average energy resolution of the same detector groups is shown in fig. 4 for the 662- and 1332-keV γ-rays. A correlation between timing and energy resolution is clearly seen: detectors that have good timing tend also to show good energy resolution. The energy resolution is not sensitive to the high voltage, but it deteriorates somewhat at very high counting rates. For counting rates below 50000 c/s, less than 0.1 % increase in energy resolution at 662 keV was observed. The pulse height for the 662 keV

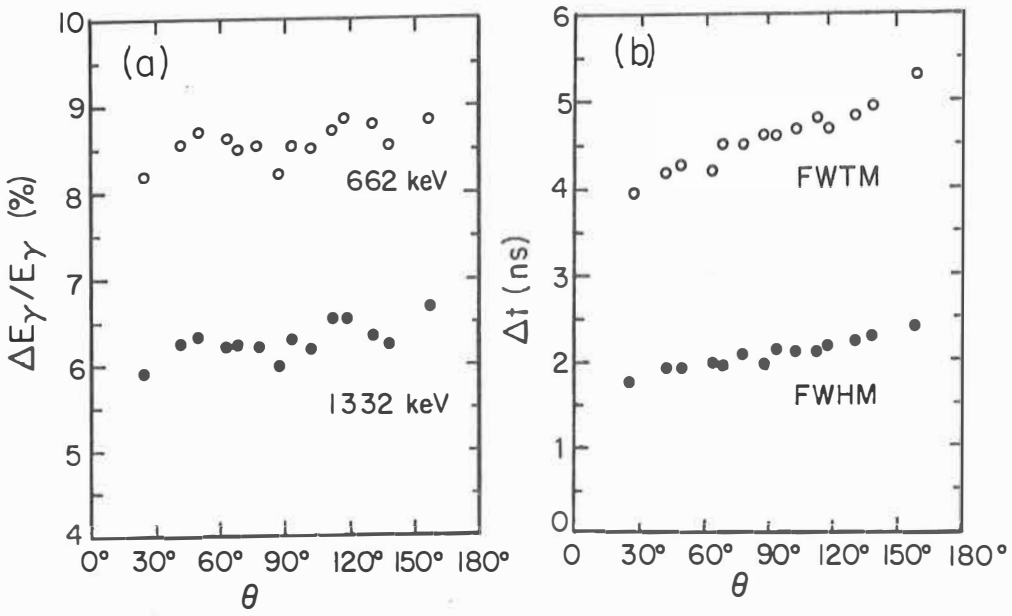

Fig. 4. (a) Energy resolution averaged over each group of 5 detectors at an angle θ with respect to the beam. The open circles give fwhm for 662 keV and the closed circles for 1332 keV. (b) Average timing resolution for the same detector groups. The open circles show fwtm and the closed circles fwhm. The detectors with the best timing resolutions were placed at forward angles.

line from ^{137}Cs was found to decrease by 0.3 % per ^{o}C over the ambient temperature range of 18^{o} - 24^{o} C. The maximum gain shift over a period of two weeks that was not correlated with the temperature was 1 % .

The pulse-height variation along the detector length as measured with a collimated ^{137}Cs source was less than 3 % on the average.

2.3. Electronics and data acquisition

A schematic diagram for the electronics of the spectrometer [27] is shown in fig. 5. The photomultiplier anode signal is first amplified by a fast × 10 amplifier [28]. One of the two amplifier outputs is shaped to an approximately triangular pulse (~ 100 ns fwhm and ~ 200 ns fwtm), attenuated, delayed by ~ 300 ns, and then fed into a charge-integrating CAMAC ADC [29]. The second output of the × 10 amplifier is

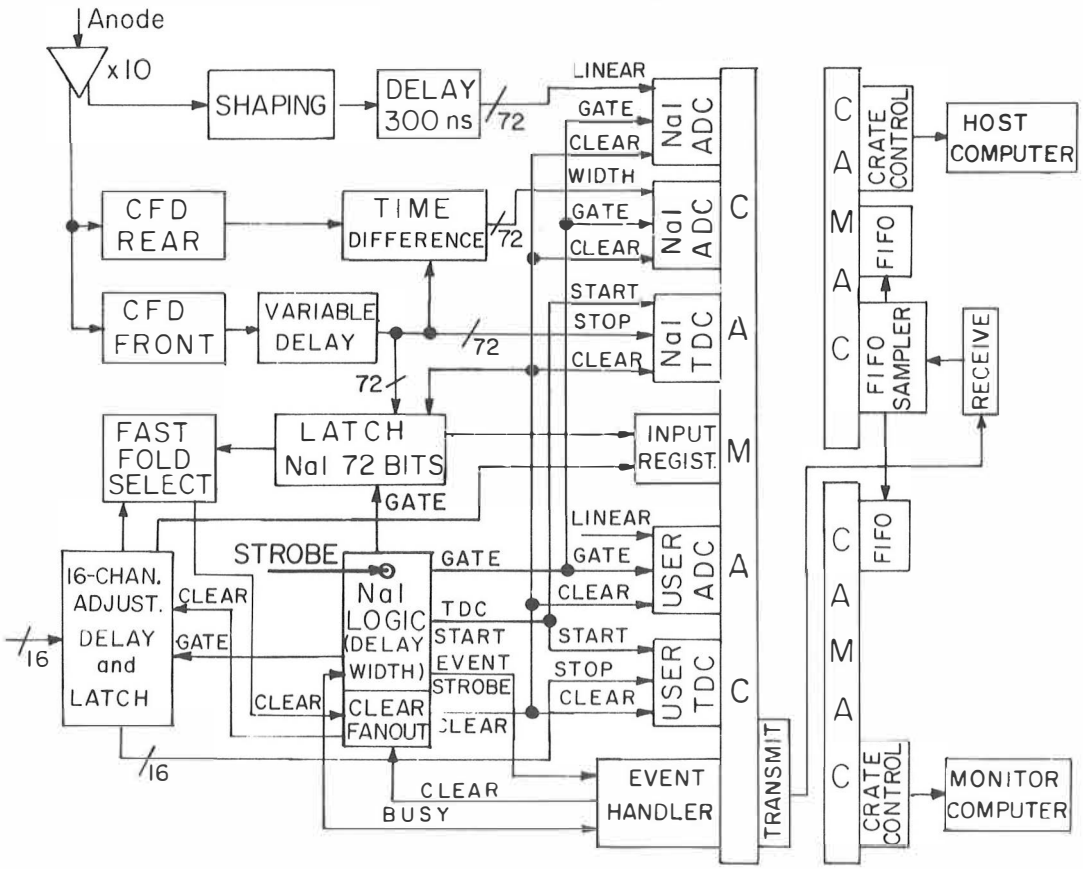

Fig. 5. Schematic diagram of the electronics.

used to establish the timing of the anode pulses by means of two constant-fraction discriminators (CFD) of special design that examine the rising and falling of the NaI pulses.

The front-edge CFD establishes the basic timing for each pulse. The time difference between the front-edge and the rear-edge triggers provides information about possible pile up or coincidence summing between a neutron and a γ-ray pulse in the same detector. The outputs of the two CFDs generate a fixed amplitude pulse with a variable width, which is proportional to this time difference. These variable-width pulses are digitized by a charge-integrating CAMAC ADC [29]. A second pulse occurring at a time 8 - 240 ns after the first pulse can be sensed with this technique. The output of the front-edge CFD is delayed, stops a time-to-digital converter (TDC) [30], and sets a detector identification bit in a gated latch. A 72-channel digital multiplicity summer (fast fold select in fig. 5) provides the coincidence fold for a possible fast hardware decision as to whether or not to record the event.

The entire system must be triggered by an external signal satisfying the criteria for an acceptable event. Suitable strobe signals with appropriate delay and width adjustments are generated to gate all the ADCs, start the TDCs, and gate the 72 latches for the NaI detectors. The information from any auxiliary detectors is entered via a user's module, which includes 16 independent inputs with adjustable delays. Internal signals are used to set appropriate bits in a user's gated latch and external signals are generated to stop the user's TDCs. All spectrometer ADCs and TDCs as well as ADCs and TDCs from the auxiliary detectors are interfaced in a CAMAC system. The six 16-bit words from the gated latches (72 bits for the NaI pattern, 8 bits for the fold and 16 bits for the user's gated latch) are accessed through a CAMAC input

register.

Data acquisition is managed by the Event Handler [31], a programmable CAMAC-based controller which selects events that meet the user's criteria, places them in a suitable format, and transmits them to the on-line computer for permanent recording on magnetic tape. The computer program may apply further selection, buffering, and formatting before the events are recorded, and it provides for on-line monitoring of the data. All CAMAC ADCs, TDCs and registers including these for the auxiliary detectors are interfaced via the same Event Handler. The time required for digitizing the signals, transmitting them to the computer, and recording on magnetic tape limits the data acquisition to 3000 events per second for events with average multiplicity $\sim$ 20 [27].

The operating characteristics of all NaI detectors are stored in a disk file. The setup and data-acquisition programs use this file to obtain information about detector parameters and CAMAC addresses for the electronics associated with each detector. This file can be updated by setup programs or edited by the user to suit his experimental requirements.

All detectors are operated with the same gain, typically 5.0 keV/channel, which provides a 10 MeV range with the 2048-channel ADCs. The gains are set by a computer program that adjusts the phototube voltage on the basis of spectra for a γ-ray source with two well-separated lines (for example, ^{88}Y). A peak search routine determines the location of the selected lines and the voltages required to give the desired gain are calculated. The phototube voltages, furnished by CAMAC-interfaced power supplies [32], are then set to these values by the computer and the process is iterated. Adjustment to $\pm$ 0.5 V (the smallest change possible with the high voltage supplies) results in gain variations of

less than 1 % between detectors. The final adjustment of gains is done in software during playback of the event tapes on the basis of post-run calibrations described later.

Checking and setting up the instrument can be accomplished with two computers, an LSI-11 microprocessor-based system and a Perkin-Elmer (PE) 3220 computer. Since the PE computer has a faster central processor unit and the tape units of highest speed and density, it is writing the events on tape. The data stream from the Event Handler is sent via a first-in-first-out buffer (FIFO) directly to one of the two computers, or it can be sent through a FIFO event sampler, which sends the complete data stream to the PE computer while allowing the LSI-11 computer to sample the event stream at its maximum capability without interfering with the writing of event tapes (see fig. 5). This feature provides flexibility for monitoring the data during acquisition. The LSI-11 can monitor either one or two parameters at a time from the complete configuration of the experiment and loop through all the detectors sequentially. A live display of the data from any two parameters can be created with 256×512 channel resolution on a storage screen or the data can be stored in memory as a 140×140 channel array. The PE computer has larger storage areas and can acquire data from all the detectors simultaneously. The acquisition programs for the PE computer provide for monitoring by creating in core or on disk one- or two-parameter arrays from all the 72×3 parameters of the spectrometer and those of the auxiliary detectors. Since the tape writing task is given the highest priority, the percentage of the total data monitored varies with the data flow rate and the number of one- or two-parameter arrays that are generated.

The Event Handler continuously monitors the status of the high-

voltage power supplies. If it detects an error condition, it halts data acquisition and generates an audio alarm to alert the experimenters.

The time scale is set approximately the same for each detector by manual adjustment of each TDC unit. The thresholds for the constant fraction discriminators are also adjusted manually. The discriminators were adjusted to minimize the dependence of timing on pulse height ("walk"). The data analysis programs allow for event-by-event correction of walk if necessary.

2.4. Calibration methods

It is of fundamental importance to predict the outcome of an event consisting of $\{E_i\}_{i=1,\ldots,M}$ γ-rays. The response of the spectrometer to this input is determined by several physical effects that depend on the geometry of the spectrometer and on the properties of the γ-cascades and other emitted penetrating radiations. The most significant effects are (i) incomplete detection of γ-rays, (ii) detector-to-detector scattering, (iii) coincidence summing in each detector element, and (iv) pulses originating from other sources, e.g., neutrons and/or high energy protons. The first three of these are connected to the detection of one or more γ-rays by one or more detectors in the spectrometer and must be taken into account quantitatively in the calibrations. Some of the γ-rays that escape detection do so through the holes in the spectrometer shell or are absorbed in the cans without encountering the scintillator. Furthermore, the shell thickness is not sufficient to absorb completely all the high-energy γ-rays or all of the secondary radiation produced in an initial interaction. The scattering from one detector to its

neighbor is appreciable due to the absence of shielding between detectors, necessary to maximize the total efficiency. The coincidence summing arises from the finite probability that more than one γ-ray from a given event may strike the same datectors, and is significant when the γ-ray multiplicity is high.

In order to achieve better resolution in multiplicity and total energy for the spectrometer, it is of great importance to discriminate against pulses which are not due to γ-rays. Most of the neutrons can be identified by their time of flight. It is also possible to distinguish between pulses arising from γ-neutron coincidence summing and those due to γ-rays by using the pulse width discrimination (see Sect. 2.3). The effect of neutrons that cannot be distinguished by these methods has to be taken into account in the data analysis. This can be done either by measuring the effective neutron response and scattering and including these in the response functions or by applying the correction on event-by-event basis using an "equal-probability separation line" for neutrons and γ-rays in a map of time of flight vs. pulse height. This method is discussed in Sect. 2.5.

Let $P(EM\,;Hk)$ be the probability for a system of N detectors to record a total pulse height H and fold k for an input event of total energy E and multiplicity M, where $H = \sum_{i=1}^{N} h_i$ is the sum of pulse heights and $E = \sum_{i=1}^{M} E_i$ is the sum over the γ-ray energies in the cascade. These probabilities are needed for transforming the observed distributions $Q_x(H\,,k)$ for any selected class of events $\underline{x}$ to the populations $R_x(E\,,M)$, or for reporting the distribution $\Delta R_x(E\,,M)$ of events that lie between H and $H + \delta H$ and have a given k. Furthermore, let $p_n(EM\,,E_\gamma : h_i)$ be the probability to register a pulse h_i in the detector element $\underline{n}$ from an input γ-ray spectrum $E_\gamma + \{E_j\}_{j=1,\ldots,M-1}$ with $E = \left(\sum_{j=1}^{M-1} E_j\right) + E_\gamma$. These

probabilities $p_n(EM, E_\gamma; h_i)$ are needed to unfold the pulse-height spectrum observed in a given NaI detector in order to obtain the associated energy spectrum.

Ignoring the angular correlation effects, analytic expressions for $P_N(EM, Hk)$ have been derived in ref. [25]. In principle it is possible to obtain $P_N(EM, Hk)$ from eq. (18a) of ref. [25] using experimentally determined single-photon responses. However, the complexity of that equation makes routine evaluation of $P_N(EM, Hk)$ impractical. Expansion in terms of the first few moments is very convenient for rapid evaluation of the projections of $P_N(EM, Hk)$ on either the H or k axis, but it cannot be used for the full characterization of the exact bivariate distribution $P_N(EM, Hk)$ because that requires cross correlation terms of higher order, i.e. $\langle H^2k \rangle$, $\langle Hk^2 \rangle$, etc., which are difficult to obtain analytically. However, a complete characterization of $P_N(EM, Hk)$ can be obtained using an experimental method. The simple case of an input cascade of M γ-rays with equal energy $E_\gamma = E/M$ can be discussed first. A source emitting two γ-rays in cascade with known branching ratio as close to unity as possible can be placed in the spectrometer. A Ge detector is then used to trigger the data acquisition system, and the response of the entire spectrometer is recorded on magnetic tape by writing in an event-by-event mode all the pulse heights and associated times of the detectors that fire. On the playback of the event data, observation of a pulse in the Ge detector in the photopeak of one of the γ-rays ensures that the second γ-ray was actually emitted inside the spectrometer in that event. By scanning the event data it is possible to construct the full single-photon and the multiple-photon responses for the spectrometer as described below.

2.4.1. Single-photon response parameters

The single triggering efficiency for an incident photon of energy E_γ, is defined as

$$(1a) \qquad \Omega' \equiv \sum_{i=1} \sum_{\kappa} \Omega^{(i)}(h_\kappa)$$

where $\Omega^{(i)}(h_\kappa)$ is the probability of recording a pulse height h_κ in the i^{th} detector, when no other detector responds. If all detectors are taken as equivalent then $\Omega' = N \sum_{\kappa} \Omega(h_\kappa)$. Similarly, the double-triggering efficiency is

$$(1b) \qquad \Omega'' \equiv \sum_{ij} \sum_{\kappa\lambda} \Omega^{(ij)}(h_\kappa h_\lambda) = N(N-1) \sum_{\kappa\lambda} \Omega(h_\kappa h_\lambda),$$

and the triple-triggering efficiency is

$$(1c) \qquad \Omega''' = \sum_{ijk} \sum_{\kappa\lambda\mu} \Omega^{(ijk)}(h_\kappa h_\lambda h_\mu) = N(N-1)(N-2) \sum_{\kappa\lambda\mu} \Omega(h_\kappa h_\lambda h_\mu) ,$$

where $\Omega^{(ij)}(h_\kappa h_\lambda)$, and $\Omega^{(ijk)}(h_\kappa h_\lambda h_\mu)$ are the probabilities for recording pulse heights $h_\kappa h_\lambda h_\mu$ in the ijk detectors, respectively; $\Omega(h_\kappa h_\lambda)$ and $\Omega(h_\kappa h_\lambda h_\mu)$ are the probabilities for recording pulse heights $h_\kappa h_\lambda h_\mu$ averaged over all detector elements. The total triggering efficiency Ω_T is defined as

$$(2) \qquad \Omega_T = \Omega' + \Omega'' + \Omega''' + \ldots$$

Clearly, $1 - \Omega_T$ is the probability for no response. In eqs. (1a - c) each multiple event must be counted only once.

Calibration measurements are taken with the following γ-ray sources: ^{75}Se (136 - 265 keV cascade), ^{207}Bi (1064 - 570 keV cascade), ^{60}Co (1173 - 1332 keV cascade), ^{88}Y (898 - 1836 keV cascade), and ^{24}Na (2754 - 1369 keV cascade). The results for Ω_T, Ω', Ω'' and Ω''' corrected for random events, branching ratios and internal conversion are shown in fig. 6 for calibration with 69 detectors in the spectrometer. It is seen that Ω'' rises rapidly above $\sim$ 300 keV, levels off and reaches the value of 0.30 at 2754 keV, whereas Ω''' is small up to $\sim$ 2 MeV (< 0.03), but above this energy it increases rapidly.

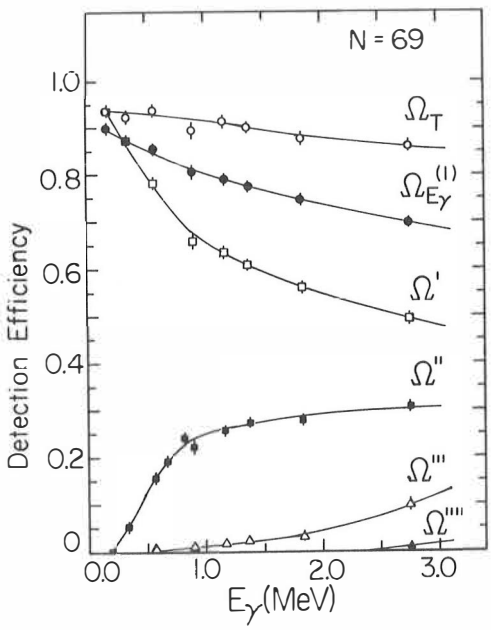

Fig. 6. Measured detection efficiencies for a setup with 69 detectors. The open squares, closed squares, open triangles and closed triangles give the triggering efficiencies for 1-, 2-, 3- and 4-fold events, respectively, from monoenergetic γ-rays as a function of γ-ray energy. The open circles give the total triggering efficiency. The closed circles give the fraction of γ-ray energy deposited in the entire spectrometer.

The double and triple scattering factors $F'' = \Omega''/\Omega_T$ and $F''' \equiv \Omega'''/\Omega_T$ are defined so that

(3) $$\Omega' = \Omega_T (1 - F'' - F''' - \ldots) = \Omega_T (1 - F),$$

where

(4) $$F = F'' + F''' + \ldots$$

The angular dependence of the two-fold scattering is given by

(5) $$F_i''(\theta) = \sum_j \Omega''_{ij}/\Omega_T,$$

where Ω''_{ij} is defined as $\Omega''_{ij} = \sum_{\kappa\lambda} \Omega^{(ij)}(h_\kappa h_\lambda)$ and the summation is over a subgroup of detectors having an angle θ with the i^{th} one. If the i detector is taken to be one of the pentagonal elements in the spectrometer, then there are 14 groups of 5 detectors forming the same angle. It is worth pointing out that for the 834 keV γ-rays about 72 % of the detector-to-detector scattering is concentrated among the five nearest neighbors [33]. For $\theta \gtrsim 60^o$ the scattering is very small and essentially independent of the angle.

The scattering factors F , F'', F''' , etc. defined in eq. (4) permit evaluation of the efficiencies Ω', Ω'', Ω''' etc. from the total triggering efficiency Ω_T via eqs. (3) and (4). Another important quantity is the fold scattering factor F_k, which is defined as

(6) $$F_k \equiv F'' + 2F''' + 3F'''' + \ldots$$

$$= \frac{\Omega'' + 2\Omega''' + 3\Omega'''' + \ldots}{\Omega_T} .$$

Knowledge of F_k permits one to calculate the average number of detectors that fire for an input of M γ-rays when the total triggering efficiency is Ω_T.

With the above definition the average fold can be obtained as

$$(7) \qquad \langle k \rangle = N \{ 1 - [1 - \frac{\Omega_T(1 + F_k)}{N}]^M \} .$$

The corrected total triggering efficiency $\Omega_T(1 + F_k)$ can be expressed in terms of Ω', Ω'', ... by using eqs. (2) and (6):

$$(8) \qquad \Omega_T(1 + F_k) = \Omega' + 2\Omega'' + 3\Omega''' + \ldots$$

Expression (7) is applicable only to a cascade of M equal-energy γ-rays. For a cascade of M γ-rays with energies $\{E_\kappa\}_{\kappa=1,\ldots M}$ it should be written as

$$(9) \qquad \langle k \rangle = N \{ 1 - \prod_{\kappa=1}^{M} [1 - \frac{\Omega_T(1 + F_k)}{N}]_\kappa \}$$

where the efficiencies in parentheses are evaluated at the appropriate transition energies E_κ. Clearly $\Omega_T(1 + F_k)$ can be larger than unity for sufficiently large values of F_k. Using the values from the smooth curves drawn through the data of fig. 6 the results for $\Omega_T(1 + F_k)$ shown in fig. 7 can be obtained. The rapid increase observed over the energy range from 300 - 800 keV is associated with the sharp rise of Ω'' observed over the same energy range. From 1.0 to 2.2 MeV $\Omega_T(1 + F_k)$ is essentially independent of energy. The large size of the individual detectors in the spectrometer suppresses considerably the double escape peaks in the spectra of the individual detectors. In most heavy-ion fusion reactions

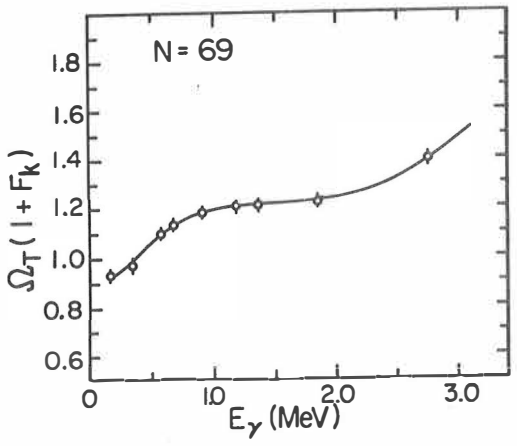

Fig. 7. Measured total triggering efficiency corrected to include detector-to-detector scattering as a function of γ-ray energy. For all but the first two points, the increase in the number of triggers due to scattering exceeds the losses due to undetected γ-rays, thus causing the corrected triggering efficiency to exceed unity.

practically all of the entry-state population occurs for values of (E/M) within the flat portion of $\Omega_T(1+F_k)$ in fig. 7. Thus approximate but realistic calculations can be made with $\Omega_T(1+F_k) = 1.22$.

The validity of the equal-energy approximation can be examined using the functions in figs. 6 and 7. As an example a cascade consisting of the yrast band in ^{160}Yb up to J = 28 [34] extended to J = 60 assuming a rotational spectrum given by $E_\gamma = \left(\frac{4J-2}{132}\right)$ MeV can be studied. A total energy of E = 30.0 MeV at M = 30 is thus obtained. Using eq. (9) $\langle k \rangle = 27.6$ is obtained. The equal-energy approximation gives, according to eq. (7), $\langle k \rangle = 28.6$. This 3.6 % difference is due to the presence of 13 transitions in the region below 800 keV, where $\Omega_T(1+F_k)$ increases rapidly with energy.

The spectral functions characterize completely the moments of the $P_N(EM, H_k)$ response with respect to the total pulse height H. The spectral functions $\omega_\ell(E_\gamma)$ are defined by

$$(10) \qquad \omega_{\ell}(E_{\gamma}) = \sum_{\lambda} \Omega_{H}(E_{\gamma}, H_{\lambda}) \cdot H_{\lambda}^{\ell}$$

where $\Omega_H(E_\gamma, H_\lambda)$ is the efficiency of the entire spectrometer to record a total pulse height H_λ from an incident γ-ray of energy E_γ. In fig. 8b spectra recorded with the entire spectrometer for the indicated incident γ-ray energies are shown. These spectra give the efficiencies $\Omega_H(E_\gamma, h_\lambda)$ which in turn characterize completely the spectral functions in eq. (10). For comparison, fig. 8a shows the pulse-height spectra $\Omega_F(E_\gamma, h_\kappa)$ from the individual NaI detectors in the spectrometer, for the same incident γ-ray energies as indicated. The efficiency $\Omega_H(E_\gamma, H_\kappa)$ is the sum of the pulse-height spectra $\Omega_{E_\gamma}^{(i)}(E_\gamma, h_i)$ of all the NaI detectors (i) from 1 to N. The spectra of fig. 8 differ from those defined by $\Omega^{(i)}(h_\kappa)$ in eq. (1) because they include the scattering from the other detectors in the spectrometer. Clearly

$$(11) \qquad \Omega_T(1 + F_k) = \sum_{\kappa} \Omega_F(E_\gamma, h_\kappa) = \sum_{i=1}^{N} \sum_{\kappa} \Omega_F^{(i)}(E_\gamma, h_\kappa) \; .$$

A set of generalized efficiencies $\Omega_{E_\gamma}^{(\ell)}$ may be defined by

$$(12) \qquad \Omega_{E_\gamma}^{(\ell)} = \omega_{\ell}(E_\gamma)/E_\gamma^{\ell} \, ,$$

where, for example $\Omega_{E_\gamma}^{(0)}$ is the triggering efficiency Ω_T and $\Omega_{E_\gamma}^{(1)}$ gives the fraction of the energy recorded by the entire spectrometer for an incident γ-ray of energy E_γ. The efficiencies $\Omega_{E_\gamma}^{(\ell)}$ decrease with increasing ℓ for constant E_γ [25].

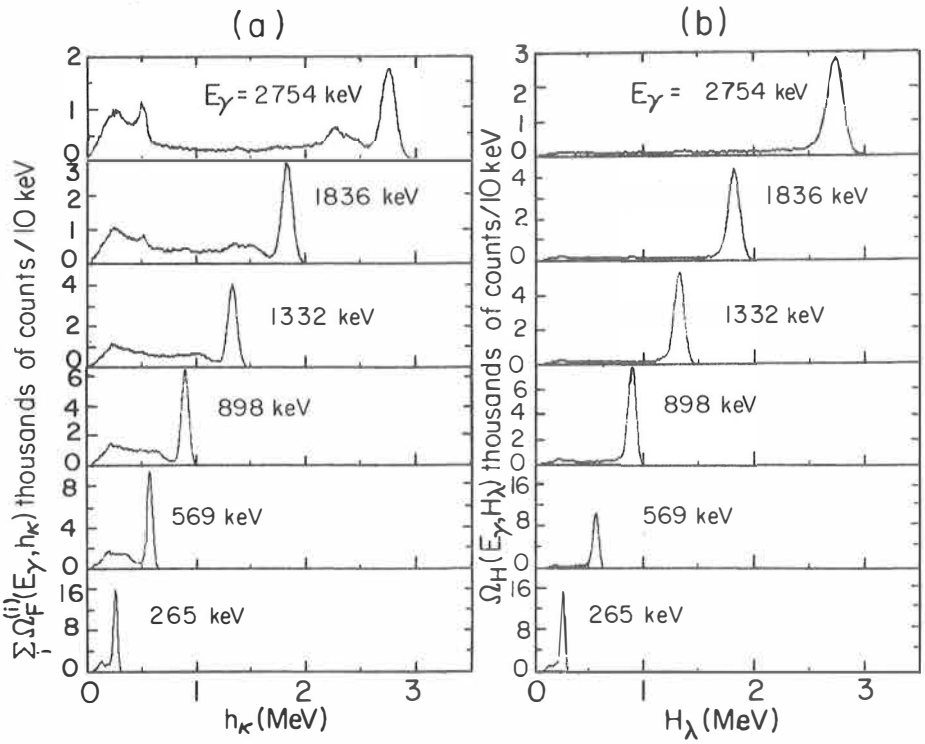

Fig. 8. (a) Pulse-height spectra recorded with individual NaI detectors in the spectrometer for each of the incident γ-ray energies indicated. These give the efficiencies $\sum_i \Omega_F^{(i)}(E_\gamma, h_\kappa)$ in thousands of counts/10 keV for 50 000 incident photons. (b) Total pulse-height spectra recorded with the entire spectrometer for the indicated incident energies. These give $\Omega_H(E_\gamma, H_\lambda)$ in thousands of counts/10 keV for 50 000 incident photons as in (a).

The generalized efficiencies $\Omega_{E_\gamma}^{(\ell)}$ for ℓ = 1, 2, and 3 obtained from the data of fig. 8 are shown in fig. 9. From these efficiencies the spectral functions $\omega_\ell(E_\gamma)$ can be computed via eq. (12). In turn,

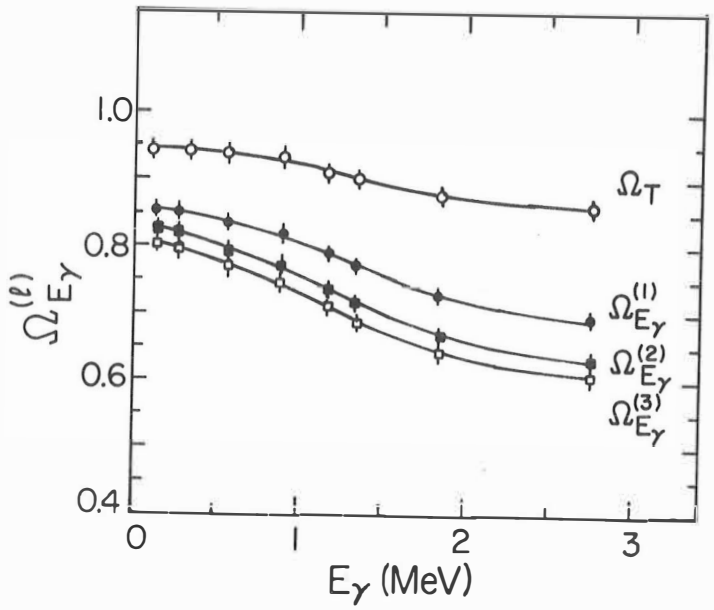

Fig. 9. Measured generalized efficiencies $\Omega_{E_\gamma}^{(\ell)}$ for ℓ = 0, 1, 2 and 3 as a function of incident γ-ray energy. Here $\Omega_T = \Omega_{E_\gamma}^{(0)}$.

the latter can be used to compute the first three moments of the projection of the response $P_N(EM, Hk)$ on the H axis. The first two moments in H are given by the following expressions, where the second equalities apply to an equal-energy cascade with $E_\gamma = \sum E_\kappa/M$:

$$(13) \qquad \langle H \rangle = \sum_{\kappa=1}^{M} \omega_1(E_\kappa) = M\omega_1(E_\gamma)$$

$$(14) \qquad \sigma_H^2 = \sum_{\kappa=1}^{M} [\omega_2(E_\kappa) - \omega_1(E_\kappa)^2] = M[\omega_2(E_\kappa) - \omega_1(E_\kappa)^2] \ .$$

In terms of the generalized efficiencies the first two moments $\langle H \rangle$ and σ_H^2 are given by

$$(15) \qquad \langle H \rangle = \sum_{\kappa=1}^{M} \Omega_{E_\kappa}^{(1)} E_\kappa = E \cdot \langle \Omega_{E_\gamma} \rangle ,$$

$$(16) \qquad \sigma_H^2 = \sum_{\kappa=1}^{M} (\Omega_{E_\kappa}^{(2)} - \Omega_{E_\kappa}^{(1)\,2}) \cdot E_\gamma^2$$

where $\langle \Omega_{E_\gamma} \rangle = \langle H \rangle / E$, is the average efficiency. It is useful to approximate this quantity by the efficiency $\Omega_{\langle E_\gamma \rangle}$ at the average energy $\langle E_\gamma \rangle = E/M$ for a cascade of M equal-energy γ-rays. That is

$$(17) \qquad \langle H \rangle = E \cdot \langle \Omega_{E_\gamma} \rangle \cong M \cdot \langle E_\gamma \rangle \cdot \Omega_{\langle E_\gamma \rangle} .$$

This approximation works better for the evaluation of $\langle H \rangle$ for a realistic cascade than for the evaluation of $\langle k \rangle$ for the same cascade. This is because $\Omega_{E_\gamma}^{(1)}$ varies less with E_γ (essentially linear) than $\Omega_T(1 + F_k)$. For the ^{160}Yb example given earlier, $\langle H \rangle$ = 23.9 MeV which gives $\langle \Omega_{E_\gamma} \rangle$ = 0.797 The equal-energy approximation gives $\langle H \rangle$ = 24.3 MeV or $\Omega_{\langle E_\gamma \rangle}$ = 0.810, a difference of only 1.7 %.

For a given input γ-ray spectrum $\{E_i\}_{i=1,\ldots,M}$ with $E = \sum_{i=1}^{M} E_i$ the mapping $(E, M) \rightarrow (\langle H \rangle, \langle k \rangle)$ is well defined from eqs. (13) and (9) in terms of $\Omega_{E_\gamma}^{(1)}$ and $\Omega_T = \Omega_{E_\gamma}^{(0)}$ for each γ-ray energy. In contrast, the reverse mapping $(H, k) \rightarrow (\langle E \rangle, \langle M \rangle)$ cannot be derived in general because the average cascade path associated with a given (H, k) selection is not known. However, with the equal energy approximation it is possible by the following iterative procedure to find a rapid solution incorporating the energy dependence of $\Omega_T(1 + F_k)$ (see fig. 7) and of $\Omega_{E_\gamma}^{(1)}$ (fig. 9). Assume for the first trial that $M_1 = k$, $E_1 = H/0.8$ and $E_{\gamma 1} = E_1/M_1$. From figs. 7 and 9 we obtain $[\Omega_T(1 + F_k)]_1$ and $\Omega_{E_{\gamma 1}}^{(1)}$. Using these results

and solving eq. (7) for M approximations

$$M_2 = \frac{\ln(1 - k/N)}{\ln\left\{1 - \frac{[\Omega(1 + F_k)]_1}{N}\right\}} \tag{18}$$

and $E_2 = H_1/\Omega\langle E_\gamma\rangle_1$ are obtained. Now $\langle E_\gamma\rangle_2 = E_2/M_2$. The procedure can be repeated until successive values of (E , M) do not differ significantly. For entry-state populations resulting from typical heavy-ion fusion reactions H/k varies between 0.3 and 1.8 MeV. In such cases this procedure converges rapidly, typically after two iterations.

The reverse mapping (H , k) → (<E> , <M>) can also be obtained from a complete set of reverse responses (Sec. 2.4.3).

2.4.2. Multiple-photon responses $P_N(EM , Hk)$

In order to construct the response functions $P_N(EM , Hk)$ the event data from a source with two γ-rays can be used. Data are recorded with the spectrometer triggered by a Ge detector. The event tapes are scanned with gates on the full-energy peaks in the Ge spectrum and on the prompt peak of each Ge-NaI time spectrum for the coincident events. The events in the full-energy gate ensure that the other γ-ray was emitted inside the spectrometer. The events satisfying these criteria are copied and used to create new simulated events of multiplicity M. To construct the responses for, say, M = 30 and E = 30 · E_γ (E_γ is the energy of the γ-ray that goes to the spectrometer) the new events are scanned in groups of 30. Each group has all the characteristics of a 30-photon event: some γ-rays may escape the spectrometer, some may hit the same detector more than once causing a coincident sum which is counted only once, and others may trigger several detectors. The total pulse height H is

obtained by summing the pulse heights of all the NaI elements that fired, while the fold k is given by the number of detectors that fire in each group of 30. The events with pulse heights in the Ge gate, which do not have any NaI triggers within the time gates measure the number of γ-rays that escape detection. Typically, at least 10 000 events of each multiplicity must be created. Responses for (E , M) with $E = M \cdot E_\gamma$ have been constructed for E_γ = 136, 265, 570, 898, 1173, 1332, 1369, 1836 and 2754 keV using the sources listed in Sec. 2.4.1. Responses for intermediate E values can be obtained by linear interpolation from the measured responses $P_N(E_1M , Hk)$ and $P_N(E_2M , Hk)$, where $E_1 < E < E_2$. Fig. 10 shows density plots of the responses $P_{69}(EM , Hk)$ with M = (E/1.0 MeV) for E = 5, 20, 35 and 50 MeV. Differences between the values of <k> from the responses of fig. 10 and those calculated using the $\Omega_T(1 + F_k)$ curve of fig. 7 in eq. (7) are smaller than 0.5 unit, which is well within the uncertainties in the measured efficiencies. The behavior of these

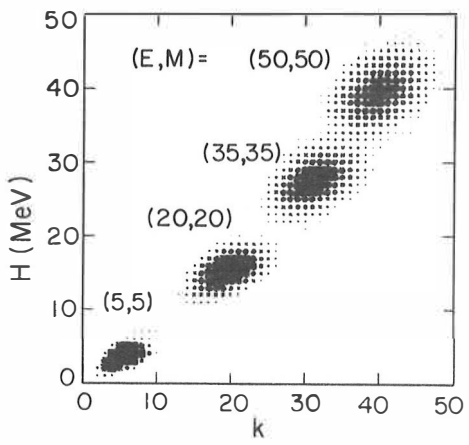

Fig. 10. Density maps of some bivariate responses $P_{69}(EM , Hk)$ obtained for the indicated values of E in MeV and M.

responses is further illustrated by their projections on the k and H axes. Fig. 11 shows the projections on the k axis (coincidence fold distributions) of the responses with E = M in MeV and M = 5, 10, 20, 30, 40, and 50. Projections on the H-axis (total pulse-height distributions) are shown in fig. 12 for M = E/(1.0 MeV) and E = 5,10, 20, 30, 40 and 50 MeV.

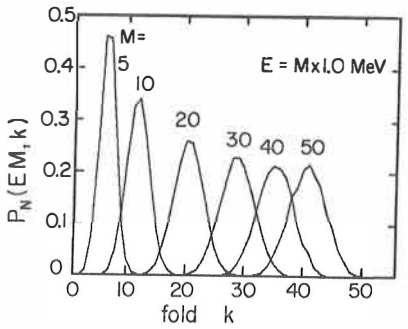

Fig. 11. Projections on the k axis of some responses measured with 69 detectors in the spectrometer for the values of E and M given by $E = M \cdot E_\gamma$ and E_γ = 1.0 MeV.

The first two moments of the distributions in H and k, shown in figs. 11 and 12, are in good agreement with the values calculated using the results of the single photon responses. The fractional resolutions $\Delta k/\langle k\rangle$ and $\Delta H/\langle H\rangle$ (where Δk and ΔH are the fwhm values) from the multiple photon responses of figs. 11 and 12 (data points) and those calculated using eqs. (22-24) and (32) of ref. [25] (smooth curves) are compared in figs. 13a and 13b, respectively. The smooth curves were calculated with the efficiency results shown in figs. 6, 7 and 9. The two methods agree well.

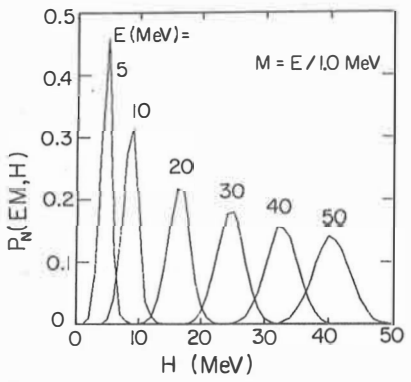

Fig. 12. Projections on the H axis of some responses obtained with 69 detectors in the spectrometer for the values of E and M given by $M = E/E_\gamma$ and $E_\gamma = 1.0$ MeV.

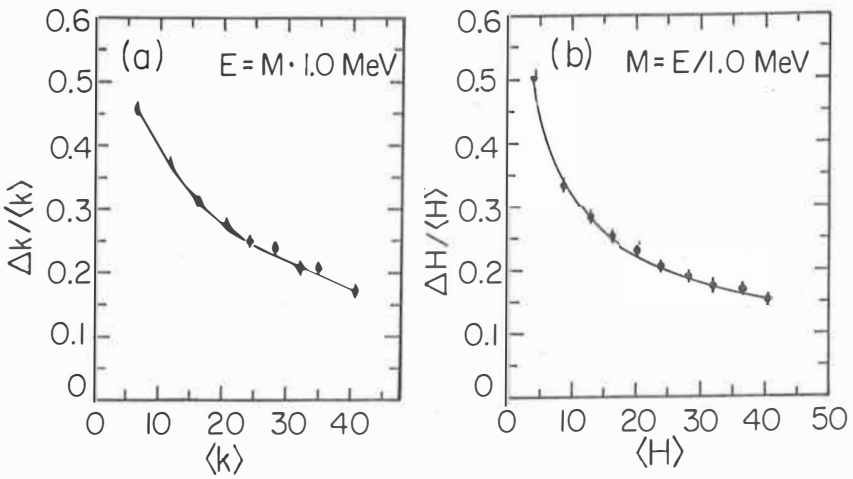

Fig. 13. (a) Fractional fold resolution (fwhm) as a function of the average fold. **(b)** Fractional total pulse height resolution (fwhm) as a function of the average total pulse height <H>.

It is clear that construction of multiplicity-M events by grouping M consecutive single events gives poorer statistics for high M. However, the total number of counts, N, recorded during calibration is usually very large (for a typical data set $N > 10^5$). Since N single events can be grouped into M events in $N!/(N-M)! \cdot M!$ ways, it is possible to use random sampling from the N events to obtain an equal number of events for every choice of M with only a very small fraction of the possible combinations being sampled. The spectral characteristics in each NaI element are well sampled with a total of $N \geq 2 \times 10^5$ counts, and this number should give an adequate description of the responses. This method for constructing the M-photon response can be extended to any given input spectrum $\{E_i\}_{i=1,\ldots,M}$. One can approximate rather well the input spectrum by a suitably weighted combination of events from different γ-ray sources, and then construct the bivariate response $P_N(EM, Hk)$ from the combined events.

The effect of the $E_\gamma = E/M$ approximation on the $\langle k \rangle$ and $\langle H \rangle$ values was discussed in Sec. 2.4.1. Also the effect on the widths Δk and ΔH can be studied. For the example of ^{160}Yb in Sec. 2.4.1 $\Delta k_{rot}/\Delta k_{E/M} = 0.974$, while $\Delta H_{rot}/\Delta H_{E/M} = 1.146$. Thus the equal-energy approximation significantly underestimates the width in H. Furthermore, for a given (E, M) point the width of $P_N(EM, Hk)$ in H for constant k is about 30 % smaller with this approximation than for this example of a rotational spectrum. The fold width, however, is in reasonable agreement.

2.4.3. Unfolding of (H, k) distributions

It is often necessary to determine the (E, M) distributions in total energy E and multiplicity M associated with the selection of events

between H and H + δH having a given coincidence fold k. For this purpose the reverse response which is the distribution in the (E , M) plane that contributes to a given point (H , k) is needed. Assuming for the moment that all (E , M) points are equally probable, the reverse responses $P_N'(Hk , EM)$ can be constructed from a complete set of responses $P_N(Hk , EM)$ by regrouping and normalizing. Normalization is important because for given E_γ dM/dk is a function of k or of M (see eq. 7):

$$\frac{dk}{dM} = - N\left(1 - \frac{k}{N}\right) \ln\left[1 - \frac{\Omega_T(1 + F_k)}{N}\right] , \tag{19}$$

whereas dE/dH is equal to $\langle \Omega_{E_\gamma} \rangle$ and thus depends only on E_γ and it is not a function of H.

The reverse responses $P_N'(Hk , EM)$ can be used to specify completely a region in (E , M) space corresponding to any (H , k) choice, provided the population distribution $R_x(E , M)$ for a class of events x is known. The selected region $\Delta R_x(E , M)$ is then obtained as the product

$$\Delta R_x(E , M) = R_x(E , M) \cdot P_N'(Hk , EM) . \tag{20}$$

Clearly the reverse responses $P_N'(Hk , EM)$ are not the inverse of $P_N(EM , Hk)$. The populations $R_x(E , M)$ must be obtained from the measured populations $Q_x(H , k)$ by solving the system of equations:

$$Q_x(H , k) = \sum_{E,M} P_N(EM , Hk)\, R_x(E , M) . \tag{21}$$

This system of equations can be solved by an iterative least-squares unfolding procedure. As an initial estimate for $R_x(E , M)$ the input data shifted by the reverse mapping $(H , k) \rightarrow (\langle E \rangle , \langle M \rangle)_1$ to the (E , M) space

is used. Since in this mapping the (<E> , <M>) values are not located exactly at the grid points of $R_x(E , M)$, the counts from each (H , k) point are distributed to a small region around the corresponding point, (<E> , <M>), using a narrow bivariate Gaussian function. The first fit $F_1(H , k)$ to the data is obtained using eq. (21) as

$$(22) \qquad F_1(H , k) = \sum_{E,M} P_N(EM , Hk)\ R_1(E , M) .$$

The fit $F_1(H , k)$ is compared point by point with the data and a ratio matrix is calculated as $B_1(H , k) = R_1(<E> , <M>)/F_1(H , k)$, where the values $R_1(<E> , <M>)$ are connected to $B_1(H , k)$ via the reverse mapping. The first estimate is then multiplied point by point by each of the reverse responses $P_N'(HK , EM)$ to give

$$(23) \qquad P_N''(Hk , EM) = R_1(E , M)\ P_N'(Hk , EM)/ \sum_{E,M} R_1(E , M)$$

The centroids of these new reverse responses, $P_N''(Hk , EM)$, provide now a better estimate for the reverse mapping. The second estimate $R_2(E , M)$ is obtained next by multiplying the data $Q_x(H , k)$ by $B_1(H , k)$ according to the mapping $(H , k) \rightarrow (<E> , <M>)_2$ from the reverse response $P_N''(Hk , EM)$. If desired, a second improvement in the reverse mapping may be derived by calculating new reverse responses as $P_N'''(Hk , EM) = R_2(E , M)*P_N'(Hk , EM)/ \sum_{E,M} R_2(E , M)$. The procedure is repeated until a minimum in the chi-square for the fit to the data is obtained. Usually this is achieved after two iterations with adjusted reverse mapping and one or two additional iterations with fixed mapping.

2.4.4. Spectral response of a single NaI detector

The energy spectrum of γ-rays for a given class of events, e.g. those associated with a given (H , k) selection, can be studied by placing a separate NaI detector outside the spectrometer to record the pulse-height spectrum coincident with the spectrometer and the triggering device(s). The large distance of the separate detector combined with appropriate shielding ensures absence of coincidence summing or crystal-to-crystal scattering. In this way the associated energy spectrum can be derived by unfolding the pulse height spectrum using appropriate single-photon responses for the outside detector. At the maximum resolving power of the spectrometer, i.e. events between H and H + δH with δH = 1.0 MeV and a single value of k, such measurements always suffer from poor statistics. A spectrum recorded with one detector in the spectrometer offers $\sim$ 11 times better statistics compared to, say, a 12.7-cm diameter by 15.2-cm long NaI detector at 90 cm from the target. By adding the spectra from all 70 elements, one obtains $\sim$ 760 times more counts. This makes it highly desirable to measure γ-ray spectra with the detectors in the spectrometer. In order to do this, however, one must apply corrections for coincidence summing and for detector-to-detector scattering because these effects distort the observed spectra considerably. These corrections can be applied to the observed pulse-height spectra or they can be incorporated into the single photon responses for each detector. The latter approach has been taken in this work. The effect of scattering is easily determined quantitatively, by noting that the procedure described in Sec. 2.4.1 for obtaining the single-photon response parameters also provides the spectra that include the scattering from the calibration sources.

The effect of coincidence summing is a function of the γ-ray multiplicity, M, and of the shape of the observed spectrum itself. The amount of summing for a given M and a total γ-ray energy E can be measured by the same method for grouping single-photon events that was used to obtain the multiple-photon responses $P_N(EM, Hk)$ in Sec. 2.4.2. The simulated events of multiplicity M can be scanned to provide the average summing as a function of M. For a given event of multiplicity M, k_h pulses in k detectors are observed ($k_h \geq k$). The differences $s = (k_h - k)$ from N events of multiplicity M show a distribution I(s). The average summing fraction is thus defined by

$$(24) \qquad S(E, M) = [\sum_S I(s) \cdot s] / M \cdot \sum_S I(s) ,$$

where $E = E_\gamma \cdot M$.

The average summing defined this way can be constructed for each calibration source. From these values a complete map for every (E, M) point can be obtained by interpolation. The average summing as a function of M is shown in fig. 14 for E_γ values of 570, 898, 1836, and 2754 keV. It is seen that in addition to the strong dependence on M, there is a dependence on γ-ray energy similar to that of $\Omega_T(1 + F_k)$ (see fig. 7).

The single-photon spectra that include the scattering can be modified to include also the summing. Clearly, the summing alters the shape of the spectrum by shifting counts to higher pulse heights and it reduces the total triggering efficiency by a factor of $[1 - f \cdot S(E, M)]$ where f is equal to 0.5 if only double summing is assumed. Let $I_{EM}(h_i)$ be a spectrum from a reaction under study associated with a total energy E and multiplicity M. Then the corrected spectral response in the n^{th} detector for a γ-ray with energy E_γ is given by

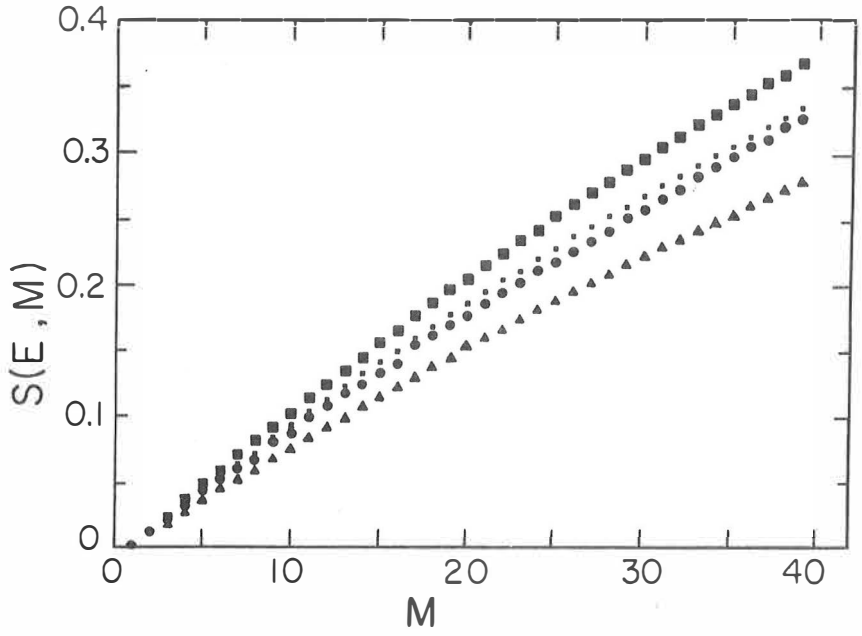

Fig. 14. Dependence of the average summing fraction S(E , M) on the multiplicity of 570 keV (triangles), 898 keV (circles), 1836 keV (small squares), and 2754 keV (large squares).

$$(25) \qquad p_n(EM, E_\gamma S; h_i) = [1 - f \cdot S(E, M)]\,\{[1 - S(E, M)]\, p_n(EM, E_\gamma; h_i)$$

$$+ \frac{1}{\sum_m I_{EM}(h_m)} \cdot \sum_{\substack{j,\ell \\ h_j + h_\ell = h_i}} S(E, M) \cdot I_{EM}(h_j) \cdot p_n(EM, E_\gamma; h_\ell)\,,$$

where $p_n(EM, E_\gamma; h_\ell)$ is the singles response for E_γ that contains the effect of scattering as described earlier. The first term in brackets is introduced to preserve the absolute calibration for the triggering efficiency.

Since the observed spectra from a reaction are directly associated with given H and k values rather than the original E and M, the summing correction can be applied only on the average by using the values for

$S(\langle E\rangle, \langle M\rangle)$ which correspond to that pair of H and k. These $\langle E\rangle$ and $\langle M\rangle$ values can in turn be obtained from the reverse mapping $(H, k) \rightarrow (\langle E\rangle, \langle M\rangle)$ described in Sect. 2.4. In order to improve the accuracy of the summing correction, the $\langle E\rangle$ and $\langle M\rangle$ values are derived from the convolution of the population $R_x(E, M)$ with the reverse responses (eq. 20).

2.5. Performance of the spectrometer

The response of the entire spectrometer to γ-rays and to neutrons from heavy ion induced reactions has been investigated in order to understand the performance of the instrument and to optimize the technique for identification of the neutrons from their time of flight.

The large cross section for inelastic scattering of neutrons on iodine and the large thickness of the NaI detectors leads up to expect large efficiency for detection of neutrons. The timing of the detectors in the spectrometer (fig. 4b) is sufficient to allow identification of the neutrons by time of flight. The energy dependence of the neutron TOF for target to interaction-point distances of 18, 27 and 38 cm is shown in fig. 12 of ref. [33]. From that figure it was deduced that pulses from neutrons with energies less than 7, 17 and 30 MeV interacting in the front, the middle or the back of an NaI element can be distinguished from γ-ray pulses.

The spectrometer has been used in experiments with the ORIC and with the 25 MV tandem accelerator at the Holifield Heavy-Ion Research Facility. The time resolution of the beam microstructure at the cyclotron is typically $\sim$ 3.5 ns, while the Tandem at present provides only a continuous beam. In order to make full use of the timing resolution of

each NaI detector, either triggering detectors with timing resolution significantly better than 2 ns must be used or the time of each event can be established from the distribution of the triggering times in the spectrometer itself. A technique based on the latter method that works satisfactorily for events with γ-ray coincidence fold $k \geq 3$ was developed.

In order to define the zero time, t_0, of a nuclear event an iterative search is initiated to identify a cluster of prompt γ-pulses. Initially, the times from all the NaI detectors are shifted by previously determined amounts to match the detectors to $\pm$ 0.2 ns. Then the times from the detectors that fired within a long interval, typically 25-50 ns, centered at the most probable time, are averaged in order to obtain the first estimate t_2 for t_0. Clearly, if some neutrons were recorded within this interval then t_2 would be too high. In the second iteration the sampling interval is reduced asymmetrically to be from t_2-10 to t_2+5 ns, and the times of the detectors firing within this interval are averaged to give t_1. Since a good part of the neutron pulses that arrive later have been left out, t_1 is a better estimate of t_0. In the third and last iteration the sampling interval is further reduced to be from t_1-4 to t_1+4 ns, and the times of the detectors within this interval are shifted so that the t_0 for that event is at some selected time t_f, which is taken to be the same for all the events. From these corrected time spectra, it is possible to decide with improved timing resolution whether each pulse was due to a neutron or a γ-ray by reference to a selected mask. The above procedure defines the t_0 of an event with an accuracy of $\Delta t/\sqrt{k}$, where Δt is the average time resolution of the k detectors that fired within the last sampling gate.

In order to demonstrate the adequacy of the t_0 technique a density map of a pulse height vs. time spectrum taken in one of the detectors at

24^{o} from an experiment with 149 MeV ^{20}Ne on ^{146}Nd is shown in fig. 15a. The starting time is derived from a Ge detector. The limited timing resolution does not permit a clear separation of the neutron events from the γ-rays. Fig. 15b shows a map of the same data with the times measured with respect to t_0 obtained as described above. The improvement is apparent. The time spectra selected through the rectangular masks indicated in fig. 15 are shown in fig. 16 and correspond to a pulse-height interval 360 - 520 keV. The upper fig. 16b is the spectrum from the corrected map.

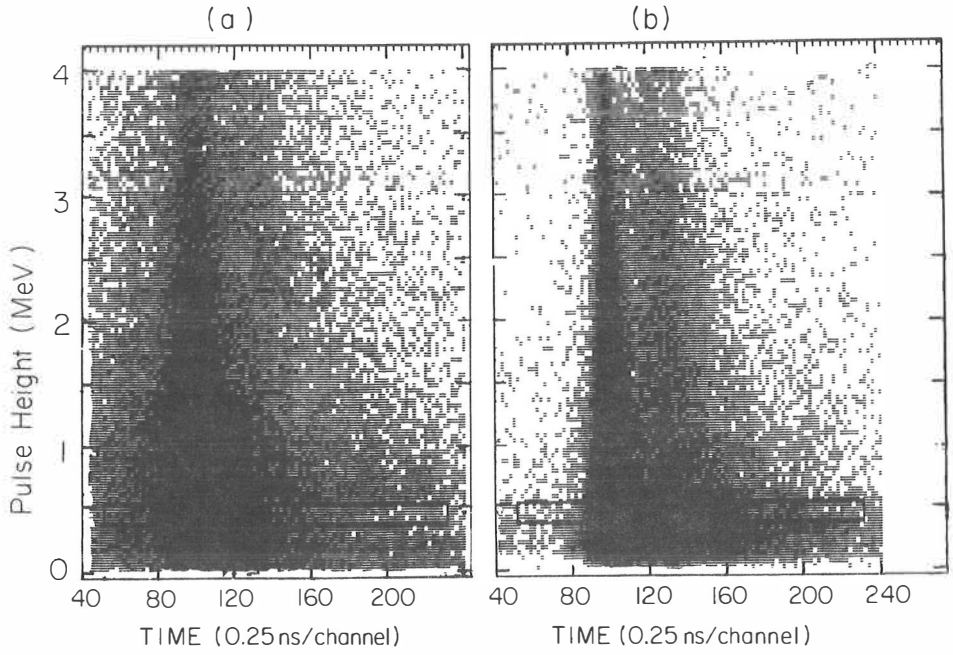

Fig. 15. (a) Density map of the observed pulse height vs. time of flight for a NaI detector at $\theta = 24.4^{o}$ triggered with a Ge(Li) detector. (b) Density map of the same data from (a) corrected by the t_0 method (see text). Prompt events are centered at time = 100. Neutrons appear at larger times.

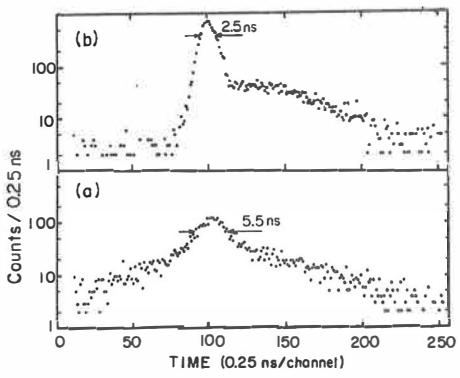

Fig. 16. (a) Time projection of the data falling in the rectangular mask of fig. 15a. The poor resolution is due to the Ge detector and does not permit neutrons to be distinguished clearly from γ-rays. (b) Time projection of the data in the mask of fig. 15b after the t_0 correction. The improved timing resolution allows the identification of practically all the neutron pulses.

In order to demonstrate further how the t_0 technique works as a function of k, in figs. 17a-e time spectra corresponding to pulse heights between 580 - 700 keV created from maps with γ-coincidence fold k_γ of 5, 10, 16, 22, and 28, respectively, are shown. These events were triggered with any count in the Ge(Li) detector without any exit channel selection. It is seen that as the fold k_γ increases the relative number of neutron pulses between 580 - 700 keV increases at first and then decreases for $k_\gamma > 10$. For this pulse-height gate and the above listed values of k_γ, the fraction of neutron pulses was found to be 31, 38, 28, 20, and 14 %, respectively. At larger pulse heights the fraction of neutron pulses increases considerably. In figs. 18f-j we show time spectra corresponding to pulse heights between 860 - 1220 keV obtained from the same maps with k_γ of 5, 10, 16, 22, and 28, respectively. The time resolution improves with increasing pulse height as indicated. For this pulse-height interval the fraction of neutrons was found to be of 29, 53, 51, 37, and 31, respectively.

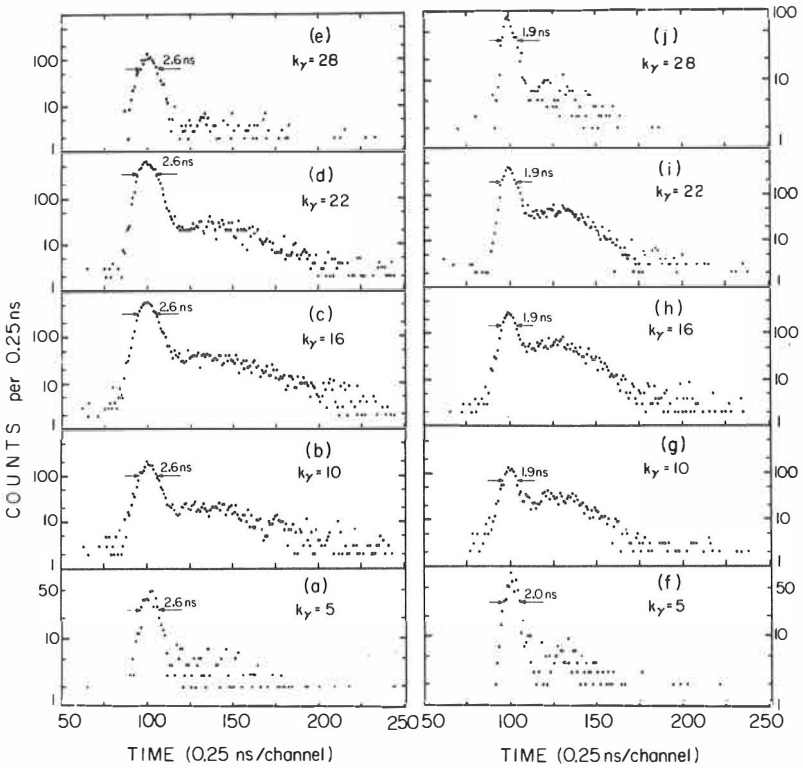

Fig. 17. (a)-(e) Time projections for pulse heights in the range of 360 - 520 keV from folds 5, 10, 16, 22, and 28, respectively. The indicated widths are fwhm. (f)-(j) Time projections for pulse heights in the range of 580 - 700 keV from the same folds. Higher pulse heights show better timing resolution.

The pulse-height spectra of the neutrons exhibit considerable line structure due to the inelastic excitation of ^{127}I and ^{23}Na in the detectors. A particularly large number of late pulses with large amplitude is observed in the h vs. t maps (see fig. 15b). The pulse-height spectra from the late pulses show a typical structure of neutron capture γ-rays

with many low-lying lines and several ones near the neutron binding energy.

The high efficiency of the spectrometer to record neutron events suggests that the distribution of the population of total neutron pulse heights H_ν should be strongly correlated with the neutron coincidence fold k_ν, in a manner similar to the total pulse height H_γ for γ-rays and their fold k_γ. The average neutron fold k_ν can be given by [15]

$$(26) \qquad \langle k_\nu \rangle = N \{ 1 - [1 - \bar{\Omega}_\nu (1 + F_\nu)]^x \}$$

where $\bar{\Omega}_\nu$ is the average detection efficiency for neutrons per detector, F_ν is the neutron scattering factor and x is the neutron multiplicity.

In fig. 18a the population $Q_\gamma(H_\gamma, k_\gamma)$ is shown from the $^{20}Ne + ^{146}Nd$ reaction at 136 MeV as a shaded contour map. The different contours correspond to decreasing factors of two going outward from the center. In fig. 18b a similar map for $Q_\nu(H_\nu, k_\nu)$ is shown. It is seen that at 1/10 maximum as many as 13 detectors respond to neutrons when the average neutron multiplicity from this reaction is $\simeq 6.2$. In fig. 18c the event-by-event correlated distribution for both neutrons and γ-rays $Q_{\gamma+\nu}(H_{\gamma+\nu}, k_{\gamma+\nu})$ is shown. The composite distribution is considerably wider along the $k_{\gamma+\nu}$ and $H_{\gamma+\nu}$ axes. The correlation of the γ-ray and neutron coincidence folds k_γ and k_ν is shown in fig. 18d. It is seen that the most probable value for k_ν corresponds to a k_γ of 20. In fig. 18e the correlation of H_ν with H_γ is shown. For $H_\gamma \geq 14$ MeV the observed H_ν values decrease with increasing H_γ.

The projections on the fold and total pulse height axis of the populations from figs 18a-c are shown in fig. 19. The closed squares, open circles and closed circles show the distributions for k_ν, k_γ, and

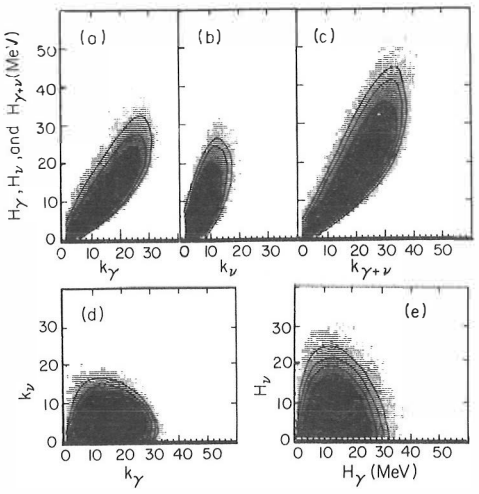

Fig. 18. Density and contour maps from the reaction of 136-MeV ^{20}Ne on ^{146}Nd before unfolding. The spectrometer was triggered by any pulse in the Ge detector. Each contour line signifies a decrease in intensity by a factor of two going outward. (a) γ-ray population $Q_\gamma(H_\gamma, k_\gamma)$. (b) Neutron distribution $Q_\nu(H_\nu, k_\nu)$. (c) Population distribution for $Q_{\gamma+\nu}(H_{\gamma+\nu}, k_{\gamma+\nu})$. It is considerably wider in both dimensions. (d) Correlation of k_ν with k_γ. (e) Correlation of H_ν with H_γ.

$k_{\gamma+\nu}$, respectively. It is clearly seen that the combined distribution for $k_{\gamma+\nu}$ is shifted upward from k_γ by ~ 6 units, which is close to the value for $\langle k_\nu \rangle$. Using the projected distribution for k_ν, and the known value of 6.2 for the neutron multiplicity, from eq. (26) $\bar{\Omega}_\nu(1 + F_\nu) = 0.0153$, which gives the value of 1.06 for the corrected total neutron-triggering efficiency $\bar{\Omega}_{T_\nu}(1 + F_\nu)$. This is comparable with the value of 1.2 for $\Omega_{T_\gamma}(1 + F_k)$ for γ-rays obtained from the flat region in fig. 7.

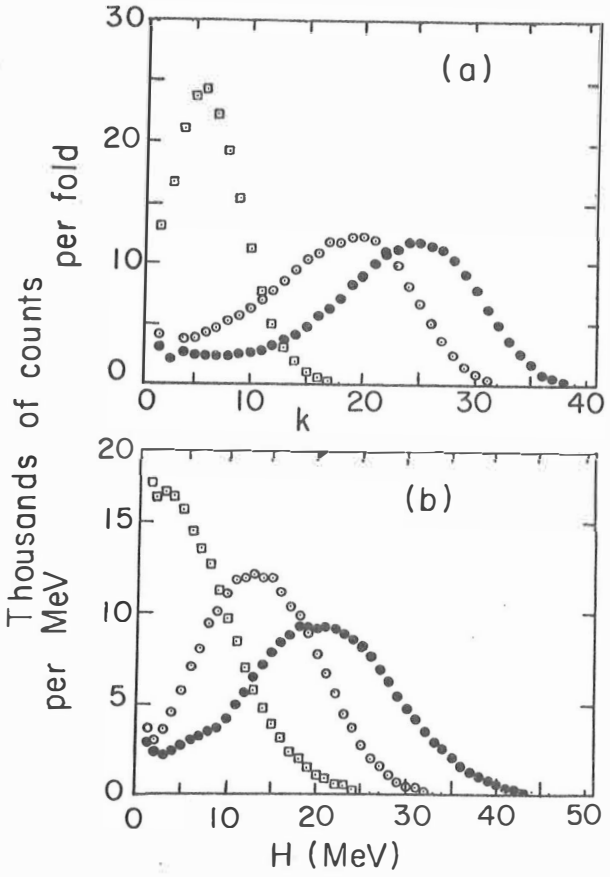

Fig. 19. (a) Fold distributions for neutrons (squares), for γ-rays (open circles) and for both neutrons and γ-rays combined (closed circles). (b) Total pulse-height distributions for neutrons (squares), for γ-rays (open circles), and for both neutrons and γ-rays combined (closed circles).

3. EXPERIMENTS WITH THE SPECTROMETER

The first experiments with the Spin Spectrometer were designed to study the heavy ion fusion reactions and the nuclear structure of transitional rare earth nuclei ($A \sim 160$) as a function of spin. The nature of heavy-ion induced fusion reactions was studied by determining the entry state populations as a function of excitation energy and γ-ray multiplicity for the product nuclei. The structure of the product nuclei up to the highest spins reached ($I \sim 55$) was studied using the continuum γ-ray decay from the entry states. In these experiments a Ge counter was used in coincidence with the entire spectrometer. In the data analysis the exit channels were selected by gating on known low-lying discrete γ-transitions in each product nucleus.

Metallic targets of ^{144}Nd (1.5 mg/cm^2) and ^{146}Nd (1.8 mg/cm^2) were bombarded with ^{20}Ne beam from ORIC. The beam energies of 136 MeV and 149 MeV were used on ^{146}Nd target and only 149 MeV was used on ^{144}Nd target. The Ge counter was positioned at 16.6^{o} with respect to the beam at the distance of 16.5 cm from the target. In this configuration 69 out of 72 NaI detectors in the spectrometer were used covering 92.3 % of 4 π. The triggering and spectral efficiencies for this setup were discussed in Sect. 2.4.1 and the multiple and single photon responses in Sects. 2.4.2 and 2.4.4, respectively. The triggering signal for the electronics of the spectrometer (Sect. 2.3) was derived from the timing signal of the Ge counter. For each event the Ge pulse height, its time relative to the cyclotron RF together with all nonzero NaI pulse heights and their times relative to the Ge trigger were recorded and written on magnetic tape. For each beam-target combination about 40 million events were recorded. This amount of high multiplicity events required about

80 tapes (1600 bpi) for each beam-target combination.

The characteristics of the spectrometer and the basic methods for data analysis were discussed in more detail in Sect. 2.4. In the first experiments the data analysis was divided into two separate steps. First the necessary calibrations were constructed from the experimental calibration data taken with radioactive γ-ray sources and the events were processed to derive the γ-ray information from the spectrometer. In this way new "prescanned" events were obtained. The second step involved the construction of the necessary spectra (post scanning) and the one and two parameter unfolding procedures.

In order to normalize the number of events and to get absolute cross-sections an absolute efficiency calibration for the Ge counter was made and the dead time corrected beam integration was done for each run.

The calibrations and the methods used in the prescanning is discussed in Sect. 3.1 and the specific methods for entry state measurements and γ-ray decay studies are described in Sect. 3.2 and 3.3, respectively.

3.1. Prescanning

During the experiment the pulse-height responses of the NaI detectors are not perfectly matched and small but different non-linearities are present. It is, however, important to correct the non-linearities and match the pulse heights of all the detectors before obtaining the total energy information or adding the γ-ray spectra from various detectors. The energy calibration for the NaI detectors was done with γ-ray sources using 10 photopeaks from 136 keV to 6129 keV. A quadratic fit

was done through the calibration points and the coefficients were used as an input for the prescanning program. The separation of the pulses due to γ-rays and neutrons was done using the time of flight information. During the prescanning the separation in each detector was determined with a mask in h_i vs. t_i (pulse height vs. time) plane. The mask for each detector was determined with the aid of two-parameter spectra (h_i vs. t_i), where the time for the NaI pulses was derived after t_0-correction as discussed in Sect. 2.5. In order to construct the masks for γ-ray pulses these spectra were sliced at constant h using 10 slices between 0.1 and 10 MeV and the valley between the γ-flash and the neutron peak was determined. The final masks were then examined also on top of an (h_i vs. t_i)-map. These masks were used as an input for the prescanning program.

After these calibration and setup procedures the original event tapes were prescanned. The prescanning procedure determined for each event the improved zero-time, t_0, separated γ-ray and neutron pulses and made the required calibrations for the NaI pulse heights in order to match the energy scales. In addition the sum of the γ-ray pulse heights (H) and the γ-ray coincidence fold (k) were determined. These were written on a new event tape together with the Ge information and the corrected NaI pulse heights (h_i) and times (t_i).

3.2. Entry state measurements

The preprocessed events were sorted to construct the population distributions, $Q_x(H, k)$, as a function of total γ-ray pulse height (H) and γ-ray coincidence fold (k) for each product nucleus separately.

These distributions were created by placing gates on the Ge photopeaks due to the $2^+ - 0^+$ or $17/2^+ - 13/2^+$ yrast transitions and the nearby background. The entry state population distributions were determined for all Yb (xn channels) and Er (α xn channels) product nuclei. Alternately, the preprocessed events were sorted to construct a Ge pulse height spectrum for each H and k. Then the areas of the photopeaks due to the $2^+ - 0^+$ or $17/2^+ - 13/2^+$ yrast transitions of the product nuclei were determined by least-squares fits with Gaussian peak shapes to provide the entry state population distributions $Q_x(H, k)$. The same results were obtained from both methods.

The entry state population distributions, $R_x(E, M)$, as a function of total γ-ray energy (E) and γ-ray multiplicity (M) were obtained from the $Q(H, k)$ distributions by solving the system of equations $\sum_{EM} P(E\ M; H\ k) \times R(E, M) = Q(H, k)$ by an iterative least-squares fitting procedure as described in Sect. 2.4.3.

The response functions of the spectrometer, $P(E\ M; H\ k)$, for M = 1 to 60 and E = 1 to 60 MeV were constructed from calibration data. The experimental calibration methods for the response of the spectrometer were discussed in Sect. 2.4.2. As shown in Sect. 2.4.2 the response functions constructed using the equal energy approximation have about 20 % narrower H projections than more realistic calculations would give. To compensate for this effect the responses were broadened before using them in the unfolding procedure. The experimental $Q_x(H, k)$ and the unfolded $R_x(E, M)$ distributions for the $^{146}Nd(^{20}Ne, 6n)^{160}Yb$ reaction at 136 MeV are shown in fig. 20.

Some of the excitation energy and angular momentum of the product nucleus are removed by low energy or delayed transitions below the gating transition (odd-A nuclei) and the gating transition itself that are not

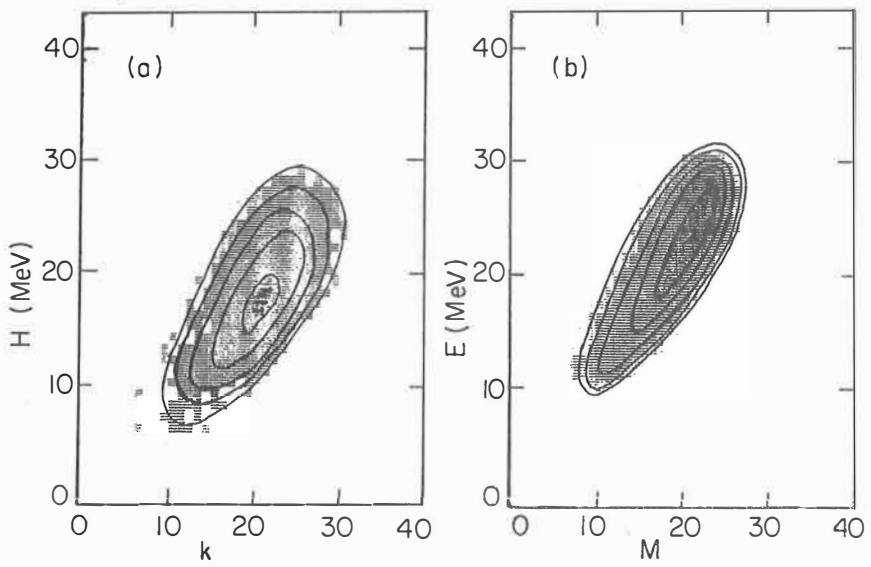

Fig. 20. (a) Measured entry state population Q(H , k) in coincidence with the 2^+ - 0^+ transition in ^{160}Yb, the 6n product from the ^{20}Ne + ^{146}Nd reaction at 136 MeV. (b) Unfolded entry state population R(E , M) from the data in (a). Adjacent contours differ by a factor of 2.

detected by the spectrometer. To correct for these effects and to make the distributions comparable the excitation energy of the 2^+ or $17/2^+$ state was added to the measured total energy and the multiplicity was increased by 1 and 3,5 units for even-A and odd-A isotopes, respectively. In addition small corrections for internal conversion and for angular correlation effects were made based on Monte Carlo simulations of the spectrometer events. The entry state populations $R_x(E^*, M)$ obtained after these corrections were compared to the statistical model calculations.

3.3. Gamma-ray decay measurements

The γ-ray decay of the entry states in $^{157-161}$Yb was studied using the NaI detectors in the spectrometer. The γ-ray pulse-height spectra for each coincidence fold and one MeV interval in total γ-ray pulse height were constructed from five different groups of detectors at the angles of 24.4^{o}, 45.6^{o}, 65.7^{o}, 77.5^{o} and 87.3^{o} (and their supplements) with respect to the beam direction. These spectra were constructed in coincidence with the $2^{+} - 0^{+}$ or $17/2^{+} - 13/2^{+}$ yrast transitions in the product nuclei observed in the Ge detector and corrected for the underlying compton background. The NaI pulse height spectra obtained this way were then added according to the selections required in each step of the data analysis as discussed later. Finally the pulse-height spectra were unfolded to yield the γ-ray energy spectra by an iterative unfolding procedure that corrects for the response of the detector. The response functions were obtained from measurements with radioactive sources of γ-ray energies between 136 keV and 4439 keV and included the effect of detector-to-detector scattering and coincidence summing appropriate for each pulse-height spectrum. These responses were discussed in more detail in Sect. 2.4.4 The associated multiplicities for each γ-ray spectrum with selected (H , k) gating were determined from the spectrometer response functions, P(E M ; H , k), the deduced entry state populations, R_x(E , M), and applied multiplicity shifts Sh(M) using the equation

$$(27) \qquad \langle M \rangle = \sum_{EM} P(E \;\; M \to H \;\; k) \times R(E , M) \cdot M / \sum_{EM} P(E \;\; M \to H \;\; k) \times R(E , M) + Sh(M) .$$

4. ANGULAR MOMENTUM IN HEAVY-ION FUSION REACTIONS

The study of the angular momentum and excitation energy dependence of fusion reactions is an important part of heavy-ion physics. The main effects manifest themselves in the population of the entry states, i.e. the states [35] in which the residual nuclei are left following the emission of particles. The spin distribution of the entry state population has earlier been studied by means of γ-ray multiplicity measurements which, in practice, have produced statistically significant information only on the first two moments of the M distribution [11,12,14]. The excitation energy distributions have most reliably been studied by measurements of particle spectra [36,37]. These experiments have given information only on the projections of the entry state populations. More recently the entry line (average E^* for each M or I) has been deduced from measurements using a γ-ray sum spectrometer [38,23]. Using the Spin Spectrometer measurements which provide detailed information on the entry state populations for different exit channels as a function of both spin and excitation energy have been done for the first time. From these data also the entrance channel ℓ-distribution leading to fusion could be determined.

In this chapter the results from the study of the heavy ion fusion using the $^{20}Ne + ^{146}Nd$ reaction at 136 MeV are reported. In Sect. 4.1 a short description of concepts of heavy-ion fusion reactions is given. The statistical model calculations and the experimental results of the entry state populations are compared in Sect. 4.2 and finally the angular momentum dependence of the fusion reactions is discussed in Sect. 4.3. In Sect. 4.4 some nuclear structure effects observable in the entry lines are discussed.

4.1. Statistical model of fusion reactions

In a complete fusion reaction the projectile and the target nucleus together form a compound nucleus. The kinetic energy in the center of the mass system is converted into excitation energy of the compound nucleus. This energy is rapidly shared by the nucleons of the compound system until the knowledge about the formation is lost. However, the conservation of total energy, total angular momentum and parity are required. The compound nucleus can decay by emission of one or more particles, γ-rays or by fission. This chain of decays continues until no particle emission is energetically possible. Then the product nucleus will decay to the ground state by γ-transitions. The decay of the compound nucleus is a statistical process that may be approximated by the methods of nuclear thermodynamics.

The maximum angular momentum of the compound system is determined by the nuclear structure and by the dynamics in the entrance channel. The upper limit due to the structure of the compound nucleus is determined by the competition between fission and particle decay. The critical value where the fission barrier vanishes is $\ell_{cr} \sim 90\ \hbar$ for $A \approx 160$ according to the rotating liquid drop model [39]. At $\ell_{cr} \sim 70\ \hbar$ the fission barrier equals the neutron binding energy. However, in the rare earth region the dynamics of the entrance channel limits the angular momentum of the compound nucleus to even lower values. The cross-section for compound nucleus formation, σ_ℓ, as a function of ℓ is

$$\sigma_\ell = \pi \lambda^2 (2\ell + 1)\, T_\ell \qquad (28)$$

where λ is the reduced wave length and T_ℓ are the transmission coeffi-

cients. For heavy-ions T_ℓ can be defined as

$$T_\ell = [1 + \exp\left(\frac{\ell - \ell_{lim}}{d}\right)]^{-1} \tag{29}$$

where d is a diffuseness parameter and ℓ_{lim} is the limiting angular momentum. The most commonly used models for calculating ℓ_{lim} are the sum rule model [40] and the Bass model [41]. The total fusion cross-section, σ_F, is

$$\sigma_F = \sum_{\ell=0}^{\infty} \sigma_\ell \,. \tag{30}$$

The transmission coefficients for light particle emission (n , p , α) can be determined using optical model potentials.

In the statistical model the compound nucleus decays via a statistical process up to the vicinity of the yrast line. After that the decay to the ground state is determined by the structure of the product nucleus. The probability for the emission of particle v from state (E_i , J_i) to state (E_f , J_f) is given by

$$P^{(v)}(E_i , J_i ; E_f , J_f) = \frac{1}{\hbar} \frac{\rho(E_f , J_f)}{\rho(E_i , J_i)} \sum_{S=|J_f-s|}^{|J_f+s|} \sum_{\ell=|J_i-S|}^{|J_i+S|} T_\ell^{(v)}(\varepsilon) \tag{31}$$

where s is the spin of the emitted particle v of energy ε and $\rho(E , J)$ is the level density. The emission probability for γ-rays of multipolarity L is given by

$$P_L^{(\gamma)}(E_i , J_i , E_f , J_f) = \frac{1}{\hbar} \xi_L^{2L+1} \frac{\rho(E_f , J_f)}{\rho(E_i , J_i)} \tag{32}$$

where ξ_L is the γ-ray strength parameter. The level density $\rho(E , J)$ is of

the form

$$(33) \qquad \rho(E, J) \propto (2J+1) \exp\{2[a(U) - E_{rot}(J))]^{\frac{1}{2}}\}$$

where $U = E - P$, P is pairing energy, $E_{rot}(J)$ is the energy at the yrast state and a is the level density parameter.

4.2. Entry state populations

The observed entry state populations, $R(E^*, M)$, for the xn channels and the total energy and multiplicity distributions summed over xn and αxn channels from the $^{20}Ne + ^{146}Nd$ reaction at 136 MeV are shown in fig. 21 and the E^* and M projections for all xn and αxn channels in fig. 22. The basicly triangular shape of the total multiplicity distribution is directly observable from the total projection as predicted by the model of fusion reactions. The energy distribution, however, is more symmetric as would be expected. Furthermore the locations of the entry state populations of different xn channels in (E^*, M) space show a qualitative agreement with the predictions of statistical model nuclear fusion reactions. Since the product nuclei of pxn channels are not known these channels together with multiple charged particle emission were not analyzed. The comparison with the statistical model calculations were based on xn and αxn channels, but this does not change the main features of the total projections significantly.

Statistical-model calculations were carried out using the Monte Carlo code JULIAN-PACE [42] further modified for more realistic treatment of γ-ray strengths . The predefined parameters for the calculations are

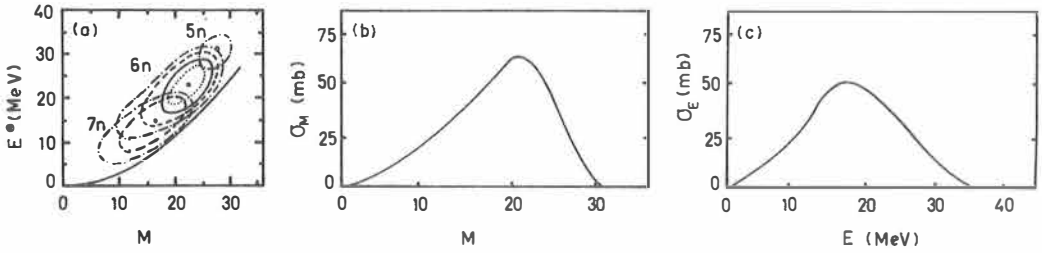

Fig. 21. (a) Contour maps of the experimental entry state populations, R(E*, M), for 5n, 6n and 7n exit channels from the ^{20}Ne + ^{146}Nd reaction at 136 MeV. The cross-section contours decrease by factors of 1.4, 2.0, 4.0 and 8.0 relative to the peak value of the 6n channel are drawn with dotted, full, dashed and dashed-dotted curves, respectively. The heavy dots locate the maximum intensity for each channel. The ^{160}Yb yrast line used in the statistical model calculations is shown by the curve below the contours. (b) Multiplicity and (c) total energy distributions summed over all xn and αxn channels.

given in ref. 32 and in references therein. The initial ℓ distribution was assumed to be of the form $(2\ell + 1)\{ 1 + \exp[(\ell - \ell_{lim})/d] \}^{-1}$ as defined in eq. 29. A reasonable agreement with the experimental data was obtained with $\ell_{lim} = 59.5$ ($\sigma_{fus} = 1138$ mb) which is a good approximation to that predicted by the sum rule model [40]. The Bass model [41] gives $\ell_{lim} = 62.6$ which is considerably too high. The diffuseness parameter, d, used in the calculations that agree reasonably with the data is between 1 and 3. The parameter value adapted for the calculations shown here was d = 2. The level density parameter was a = A/9.5. The yrast lines were taken from the rotating liquid drop model [39] above spin 22,

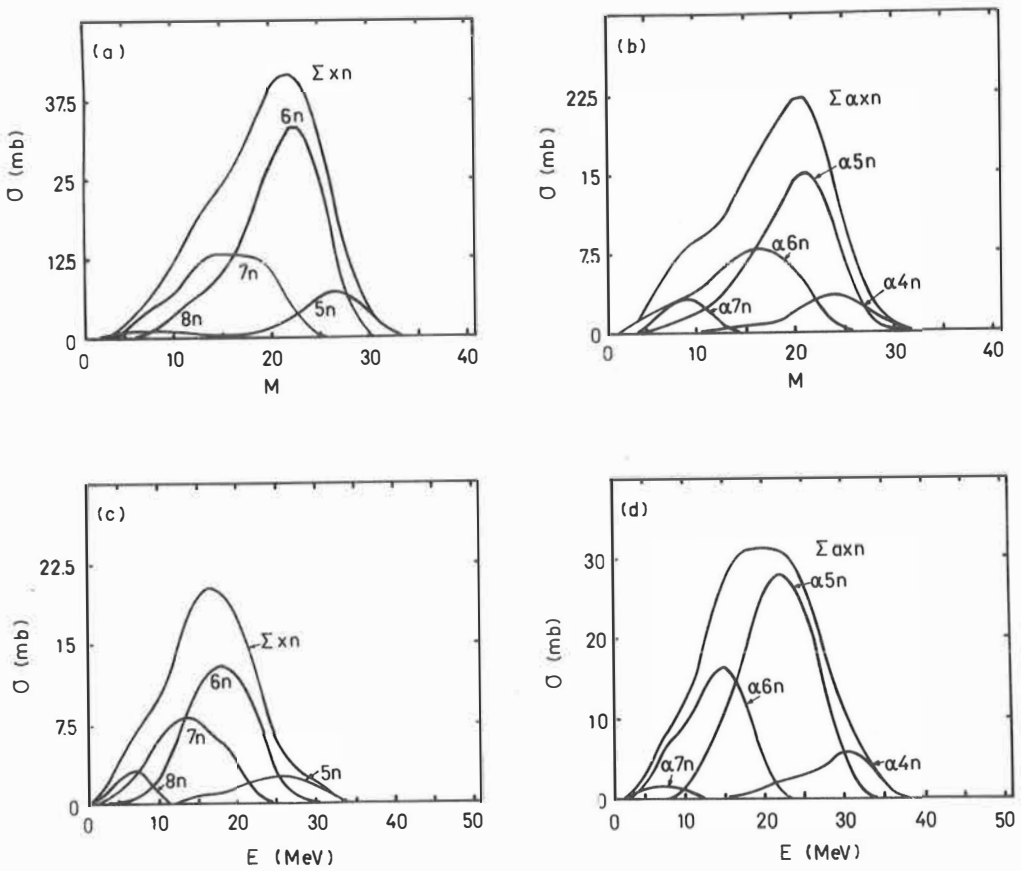

Fig. 22. Projections of the R(E*, M) distributions of different exit channels from the ^{20}Ne + ^{146}Nd reaction at 136 MeV:
(a) Multiplicity projections for xn channels
(b) Multiplicity projections for αxn channels
(c) Total energy projections for xn channels
(d) Total energy projections for αxn channels

but below that value the moment of inertia was decreased linearly with decreasing spin to approximate the behavior of rotational nuclei [8]. The E1 γ-ray emission strength included the giant dipole resonance [43-45] with its shape and position derived from experimental systematics

[46,47], and the strength determined by the energy weighted sum rule [47]. Statistical E2 and M1 transitions were included with strengths of B(E2) = 1.0 W.u. and B(M1) = 0.005 W.u., together with collective E2 transitions with B(E2) = 100 W.u. for E_γ < 2.0 MeV. The Monte Carlo γ cascades proceeded to the vicinity of the yrast line and then was assumed to reach the ground state or yrast state with I < 2 by stretched E2 transitions [42]. In these calculations information about spin and total energy as well as the γ-ray multiplicity was stored. Thus the R(E*, M) distributions were constructed and the comparison with the data was done in (E*, M) space. The multiplicity distributions for xn reaction channels are compared in fig. 23a. Fig. 23b shows the comparison of the total energy distributions.

As seen from fig. 23, a good overall agreement between the data and the statistical model calculations is obtained. This can be further confirmed from fig. 24 which shows the R_x(E*, M) distributions from xn channels for data and calculations.

As seen from figs. 23 and 24, the statistical model calculations reproduce the general features of the entry state population distributions: the cross-sections, the mean positions and the orientations of the two parameter distributions, the multiplicity and total energy projections. However, the total energy projections for a given multiplicity are about 30 % wider in the data. This discrepancy is essentially independent of the level-density parameter (from a = A/7.5 to A/10.5) and the E1 strength (from 1.0 to 1.8 times the energy weighted sum rule). However, it could be a consequence of the simplified treatment of the level densities and/or the γ-decay properties in the present statistical model calculations. However, the results from the comparison of the data and the calculations indicate that the statistical model of nuclear

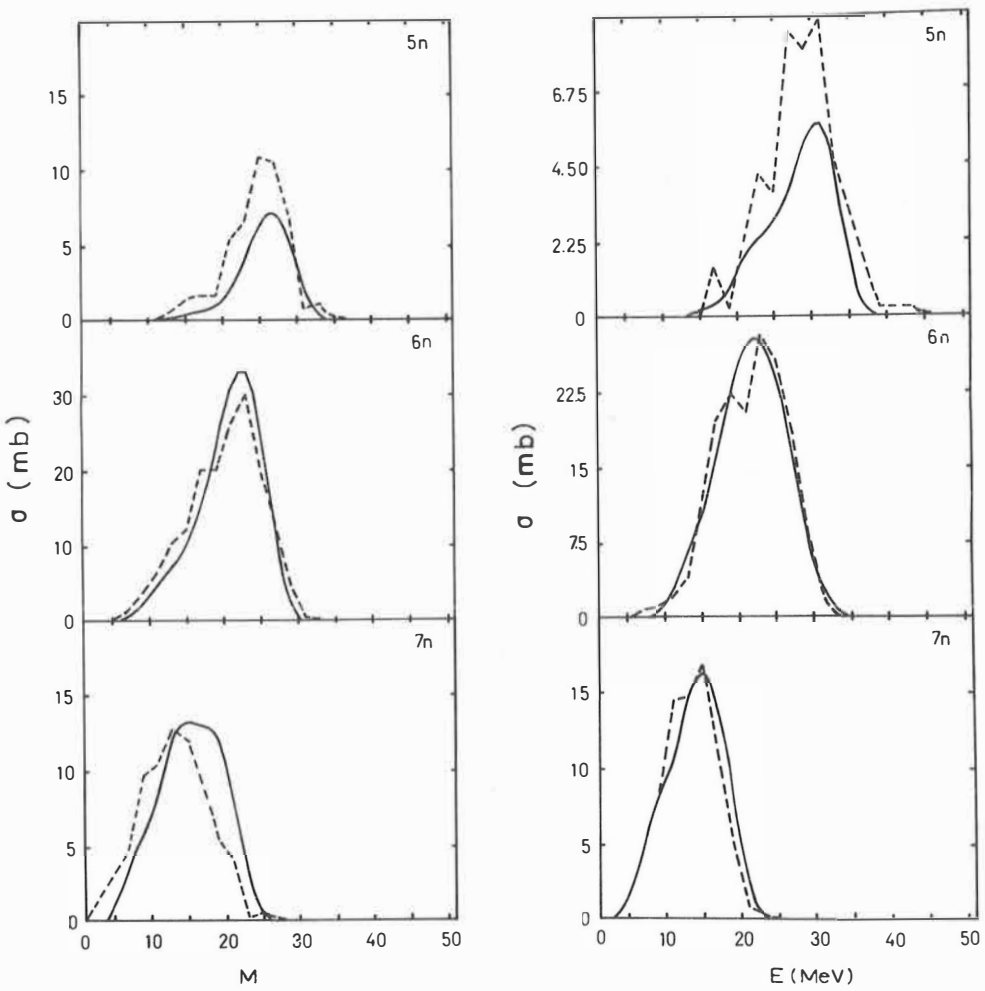

Fig. 23. Comparison of the experimental (solid line) and calculated (dashed line) (a) multiplicity and (b) total energy distributions of 5n, 6n and 7n channels.

fusion reactions can explain the main features of the mechanism but further study is needed to fully understand the detailed nuclear decay. Furthermore, the nuclear structure effects that vary from nucleus to

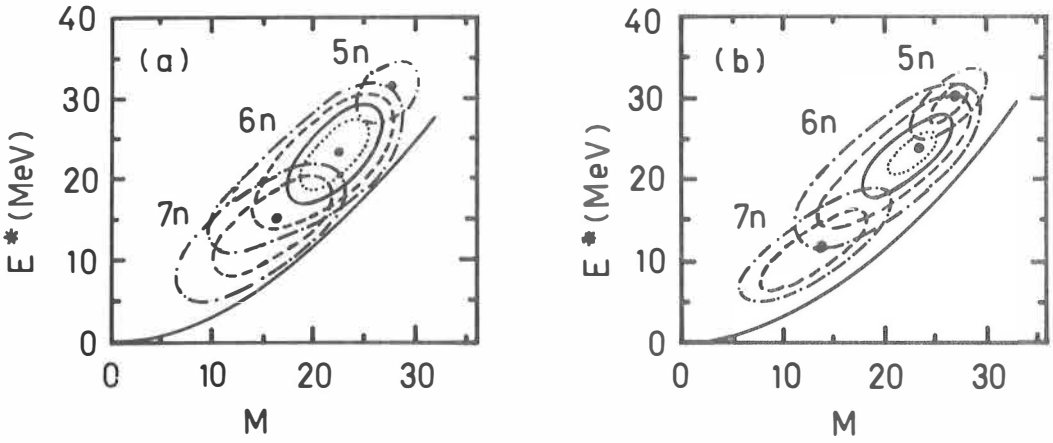

Fig. 24. Contour maps of the experimental (a) and calculated (b) entry state populations, R(E*, M) for 5n, 6n and 7n channels. The contours are as in fig. 21a.

nucleus can be significant. Thus a complete agreement between the real mechanism and the model can be achieved only if the proper knowledge about the nuclear structure of the product nuclei is incorporated. This, however, is not anymore a test for the ideas of the statistical model but a matter of application and thus related to the knowledge about the nuclear structure as a function of spin and excitation energy.

4.3. Angular momentum of the entrance channel

Since the statistical model calculations give a reasonable explanation for the observed entry state populations they provide a direct connection between the initial ℓ and the total J distribution of the product nuclei. Variations in the level density and γ-ray strengths which preserve the agreement with the data do not effect the relationship between the ℓ and J distributions significantly.

The entrance channel ℓ distribution leading to the fusion together with the total spin distribution of the product nuclei is shown in fig. 25a and the entry state populations, $R_x(E^*, J)$, for xn channels in fig. 25b. The triangular shape of the entrance channel can clearly be seen. This shape is also reflected in the spin distribution. The half height of the upper edge of the entrance channel (ℓ_{lim}) 59.5 is reduced to 51 $\hbar$ in the product nuclei due to the particle emission. The maximum moves from 56 $\hbar$ to 40 $\hbar$. Thus the diffuseness increases significantly due to the particle emission.

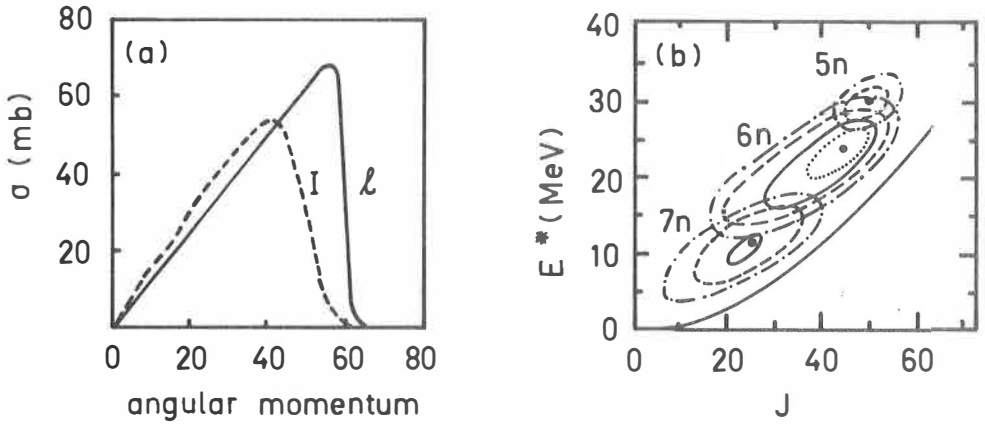

Fig. 25. (a) The entrance channel angular momentum distribution (solid line) and the spin distribution of the product nuclei after particle evaporation (dashed line) from the ^{20}Ne + ^{146}Nd reaction at 136 MeV. (b) The entry state population distributions, R(E* , J) in (E* , J) space for 5n, 6n and 7n channels. The contours are as in fig. 21.

4.4. Entry lines

A simpler way of comparing the measured and calculated populations of fig. 24 is to plot the entry lines <E*> vs. M. The entry lines for the xn channels from the ^{20}Ne + ^{146}Nd reaction at 136 MeV are shown in fig. 26 for the data (points) and the calculations (lines). Good agreement is seen for the positions and the slopes for the main part of the entry lines. However, the experimental data show a significant decrease in slope for ^{161}Yb and ^{160}Yb at M ~ 27 and 25 respectively. This effect

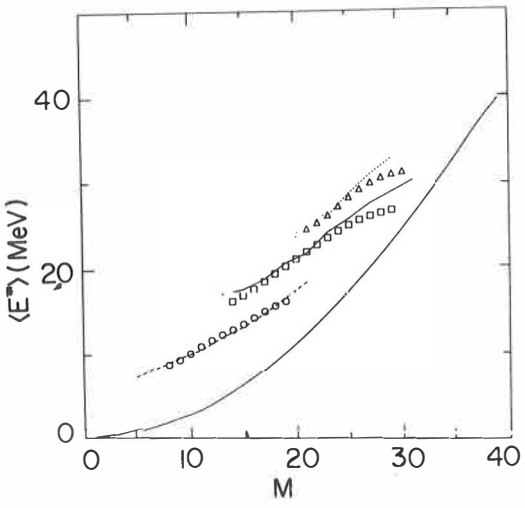

Fig. 26. Entry lines for the principal xn channels. The points represent experimental results (Δ = 5n, □ = 6n, ○ = 7n) while the lines are the results of statistical-model calculations. The lowest curve is the yrast line used in the calculations.

cannot be reproduced by the statistical model with any reasonable variation of the parameters in the model. However, a significant decrease in the slope of the yrast line (superbackbend) or a drastic change in the decay mode of the entry states for $J \gtrsim 45$ could explain the behavior. Either of these possibilities would suggest a dramatic change in the nuclear structure over a relatively narrow spin range. This change can also be responsible for the widths of the bivariate distributions.

5. GAMMA-RAY DECAY OF THE ENTRY STATES IN $^{157-161}$Yb

As seen from the study of the entry state populations in fusion reactions only a small amount of angular momentum is removed in the particle decay of the compound nucleus. Thus most of the initial angular momentum is left to the product nuclei. This character, different from all direct processes, makes the heavy-ion fusion reactions useful in the study of nuclear structure at high spin. As seen from the entry state population and entrance channel distributions (fig. 26a) discussed in Sect. 4.3 the product nuclei receive about 51 $\hbar$ units out of 60 $\hbar$ (half height of the upper edge) in the ^{20}Ne + ^{146}Nd reaction at 136 MeV. At 149 MeV bombardment the residual angular momentum increases to $\sim$ 55 $\hbar$. Since the total angular momentum distribution is fractioned between different xn channels the highest spin states are populated in the channels with fewer particles emitted as seen from the entry state populations (fig. 25b).

So far the discrete lines in most interesting nuclei are known up to I $\sim$ 30 $\hbar$ and in some cases up to I $\sim$ 40 $\hbar$ [6,7]. These states have been studied using the upper limits of the experimental method of total energy filtering. The capability of simultaneous multiplicity and total energy selection with the spectrometer can be useful in pushing these limits higher. However, the nuclei are populated above those limits and an increasing theoretical interest [9,10,48] is focused on the structure of nuclei at such high spin. Since the discrete lines cannot be resolved at very high spin nuclear structure studies must be done by observation of the unresolved (continuum) γ-ray decay of the entry states. In this chapter the decay of the entry states in $^{157-161}$Yb has been discussed. In Sect. 5.1 a short introduction to the decay of the

entry states is given. In Sect. 5.2 the general features of the continuum γ-ray spectra from the decay of the entry states in $^{157-161}$Yb are described. Some nuclear structure effects observed in the entry lines $\langle E^* \rangle$ vs. M of $^{157-161}$Yb are discussed in Sect. 5.3. The yrast like transitions in $^{159-161}$Yb and ^{157,158}Yb are discussed in more detail in Sect. 5.4 and 5.5, respectively. Finally in Sect. 5.6 different decay modes observed in these nuclei are summarized.

5.1. De-excitation of the entry states

In the de-excitation of the entry states in fusion reactions two types of γ-decay are involved. The statistical γ-rays remove mainly excitation energy essentially without changing the spin. Thus they cool the nucleus toward the yrast line. The shape of the statistical component is of the form

$$N_\gamma \propto E_\gamma^{\,n} \exp[-E_\gamma/T], \tag{34}$$

where n and T are constants depending on the entry region [8]. The yrast-like γ-rays remove more angular momentum but less energy, and decay generally parallel to the yrast line. The character of these yrast-like transitions depends strongly on the structure of the product nucleus. They can be strongly enhanced collective transitions (deformed nuclei) or of single-particle character (spherical or slightly deformed nuclei). A schematic picture of the de-excitation of the entry states is given in fig. 27. The relative number of statistical and yrast-like transitions depends on the angular momentum and excitation energy left

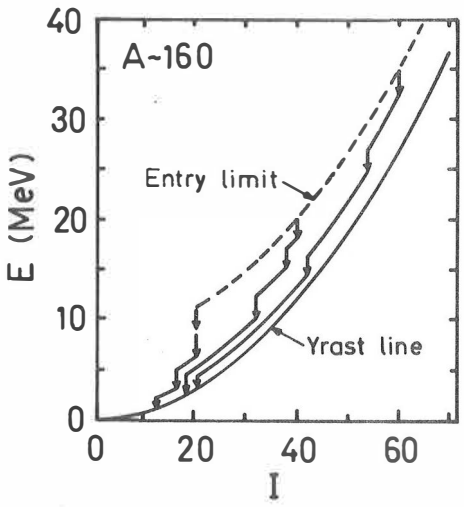

Fig. 27. A schematic γ-ray de-excitation pathway to the ground state. The statistical transitions are indicated by vertical arrows and the yrast-like transitions are roughly parallel to the yrast line.

in the final nucleus. In the case of high angular momenta the number of yrast-like transitions is much larger than that of the statistical ones. However, the absolute number of statistical γ-rays and the shape of their spectrum (n and T in eq. 34) varies as a function of excitation energy above the yrast line.

5.2. Statistical and yrast-like transitions

The unfolded continuum γ-ray spectra normalized to their respective multiplicities from the $^{144}Nd(^{20}Ne, 6n)^{158}Yb$ reaction at 149 MeV as a function of multiplicity and total γ-ray energy for selected values are shown in fig. 28. From these spectra the general features discussed in Sect. 5.1 can be seen: a bump of yrast-like transitions at $E_\gamma < 1.5$ MeV

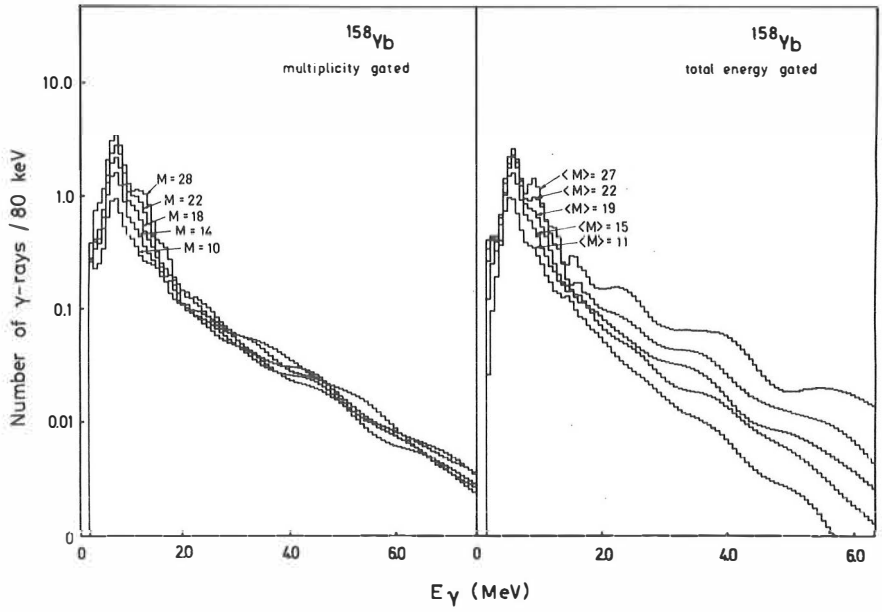

Fig. 28. The unfolded continuum γ-ray spectra from the $^{144}Nd(^{20}Ne, 6n)^{158}Yb$ reaction at 149 MeV gated with selected (a) multiplicities and (b) total energy bins of one MeV. The spectra are normalized to their respective multiplicities.

and a statistical component with exponentially falling tail. As seen from the multiplicity-gated spectra (fig. 28a) the amount of statistical γ-rays is independent of the total multiplicity. This indicates that in heavy-ion fusion reactions the number of statistical γ-rays as a function of angular momentum is constant. The spectra from other reactions and product nuclei (not shown here) confirm this observation. Also the fact that the entry lines in fig. 26 are parallel to the yrast line is in full agreement with the spectral information. This behavior helps considerably the study of yrast-like transitions using multiplicity selection of the entry region. Because the temperature and the number

of statistical γ-rays for consecutive M slices is constant the difference spectrum directly gives the additional yrast-like transitions between those slices. If a total energy selection alone is used, however, the average nuclear temperature increases rapidly as the total energy is increased. Thus the determination of the yrast-like transitions becomes very difficult and the effects observed do not have to be related to the increase in angular momentum but to the increase in excitation energy above the yrast line or a combination of these. It should be noted that the total energy selection done with the spectrometer is much cleaner than in the case of a total energy sum spectrometers because of higher efficiency and the rejection of pulses due to neutrons.

Some γ-ray spectra of the yrast-like transitions from $^{157\text{-}161}$Yb normalized to their respective multiplicities are shown in fig. 29. These spectra were constructed by summing over all detectors and the total pulse height. Thus they have only a multiplicity selection. A smooth continuous change in the structure of the γ-ray spectra in addition to the changes as a function of multiplicity can be seen when the neutron number is increased from N = 87 to 91. The structure of these spectra is discussed in more detail in Sects. 5.4 and 5.5.

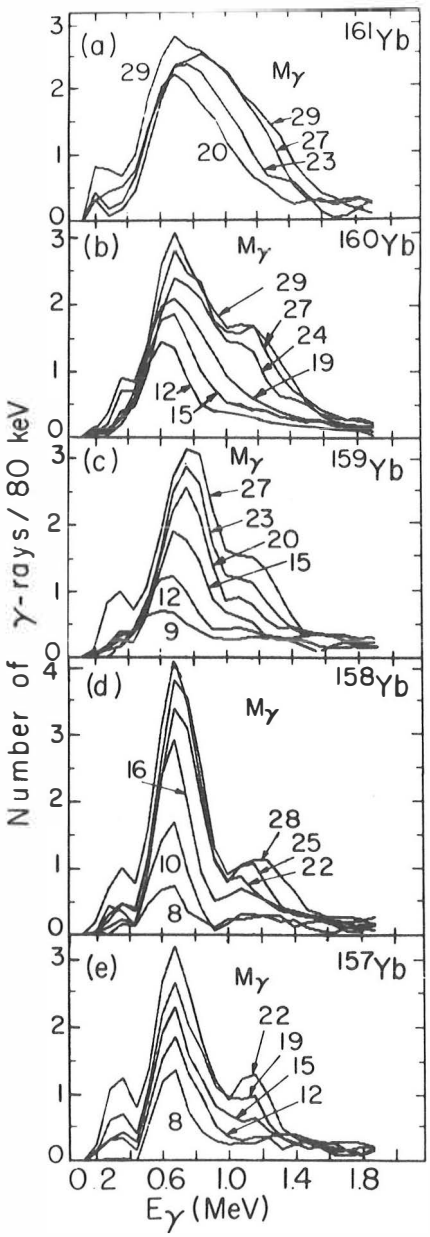

Fig. 29. Unfolded continuum γ-ray spectra of yrast-like transitions in $^{157-161}$Yb for selected multiplicities as indicated from the reactions ^{20}Ne + ^{146}Nd at 136 MeV and ^{20}Ne + ^{144}Nd at 149 MeV.

5.3. Nuclear structure effects in the entry lines

As discussed in Sect. 4.4 some nuclear structure effects cause a change in the slope of the entry lines <E*> vs. M in ^{160}Yb and ^{161}Yb at high spin. This change occurs in the lighter Yb isotopes also as seen from fig. 30, which shows the entry lines from all three reactions. The calculated entry lines for 149 MeV ^{20}Ne + ^{146}Nd data were obtained with the same set of parameters that gave the best fit to the 136 MeV data. These lie at somewhat higher than the data, but this is not significant, since no effort was made to fit the data in detail. All entry lines exhibit a significant decrease in slope at M_γ = 21, 22, 23, 25 and 27 for $^{157\text{-}161}$Yb, respectively. This change in slope depends only on the nucleus formed and not on the reaction used to produce it. This can be seen even more clearly from fig. 31 which shows the entry lines and multiplicity population distributions for ^{160}Yb from 136 MeV and 149 MeV data. The change in the slope of the entry lines occurs at M ≈ 25 for both bombarding energies although it is located in a completely different part of the population distribution. Thus the reaction effects or edge effects of the data analysis cannot be responsible for the behavior of the entry lines. ^{159}Yb does not show any changes at lower beam energy which reaches up to M ≈ 20 but has a downbent at M ≈ 23 in the 149 MeV data as seen from fig. 30. The entry line for ^{158}Yb from 149 MeV ^{20}Ne + ^{146}Nd has a downbent at M ≈ 22. In addition it has smaller upbends at M_γ ≈ 16 and 28. The systematic behavior observed in the entry lines of $^{157\text{-}161}$Yb indicates changes in the nuclear structure with increasing spin. These changes manifest themselves also in the γ-ray decay of the entry states. Each of these changes in the slopes of the entry lines correlates with a change in the observed γ-ray spectrum.

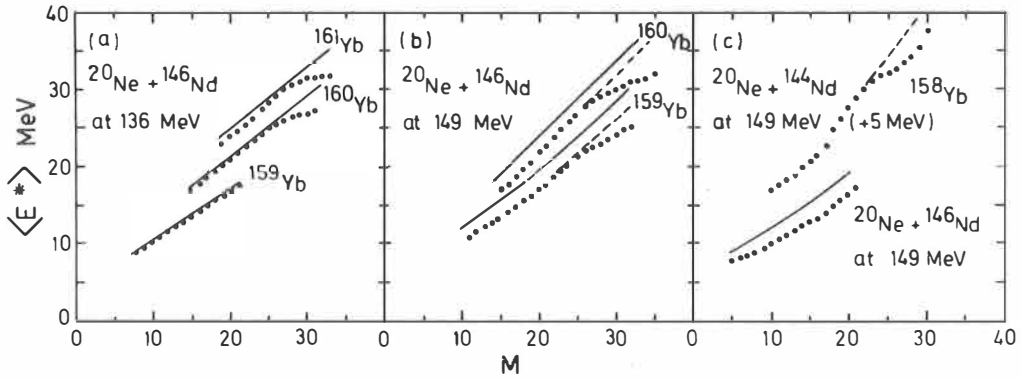

Fig. 30. Entry lines <E*> vs. M for $^{157-161}$Yb from the reactions as indicated.

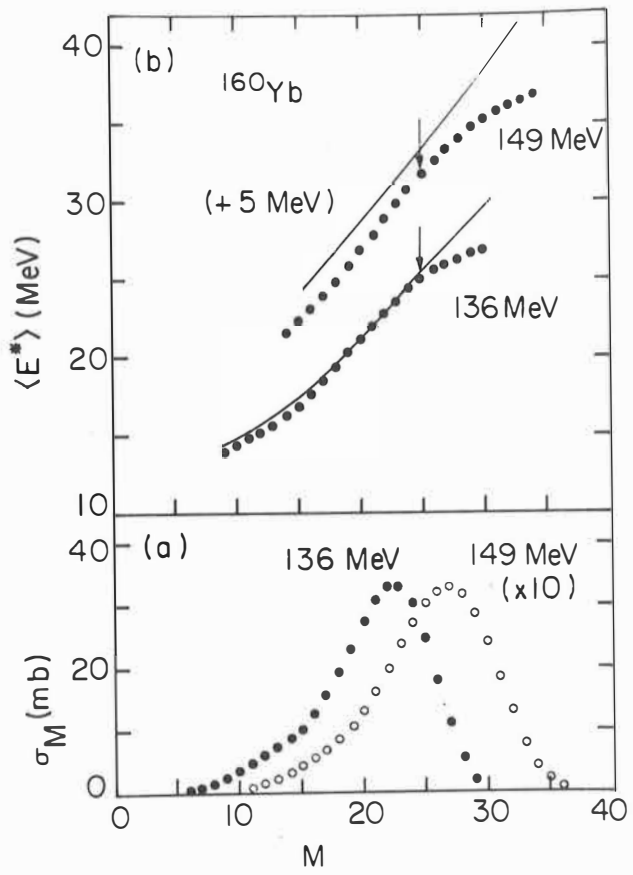

Fig. 31. Entry lines <E*> vs. M (b) and the multiplicity distributions (a) for ^{160}Yb from ^{20}Ne + ^{146}Nd reaction at 136 MeV and 149 MeV.

5.4. Yrast-like transitions in ^{161}Yb, ^{160}Yb and ^{159}Yb

The γ-ray spectra from ^{161}Yb shown in fig. 29a exhibit the expected behavior [8] for a rotational rare earth nucleus with $N \gtrsim 92$. An intensive bump with an upper edge which moves in a regular fashion to higher energies as M increases up to $M \approx 27$ is observed. The angular distribution of these γ-rays is fully consistent with an expected stretched quadrupole radiation from de-excitation of rotational states. This data also indicates a smooth behavior for the moment of inertia as a function of increasing spin.

At the highest multiplicities a new component at lower energy ($E_\gamma \approx 700$ keV) develops. Despite the presence of these localized transitions, the upper edge of the quadrupole bump (at $E_\gamma \sim 1400$ keV) continues to move to higher E_γ in the highest M_γ spectra. The onset of the localized component with an energy about half of that of the quadrupole component occurs exactly at the same multiplicity as the change in the slope of the entry line $\langle E^* \rangle$ vs. M.

The observation of these transitions also excludes the possibility of a regular rotational behavior with a rapidly increasing moment of inertia with increasing spin.

The change in the decay mode with increasing M becomes progressively more pronounced in the successively lighter Yb isotopes. In ^{160}Yb for M_γ up to 25 the spectra also show an evolving bump which for all E_γ is entirely consistent with stretched E2 transitions as seen from the anisotropies given in fig. 32a for M = 16 - 19. At M > 25 the γ-ray spectra show a localization of additional transitions at $\sim$ 650 keV and a continued but somewhat slower evolution to higher E_γ of the edge of the quadrupole bump. The transitions localized at 650 keV are clearly

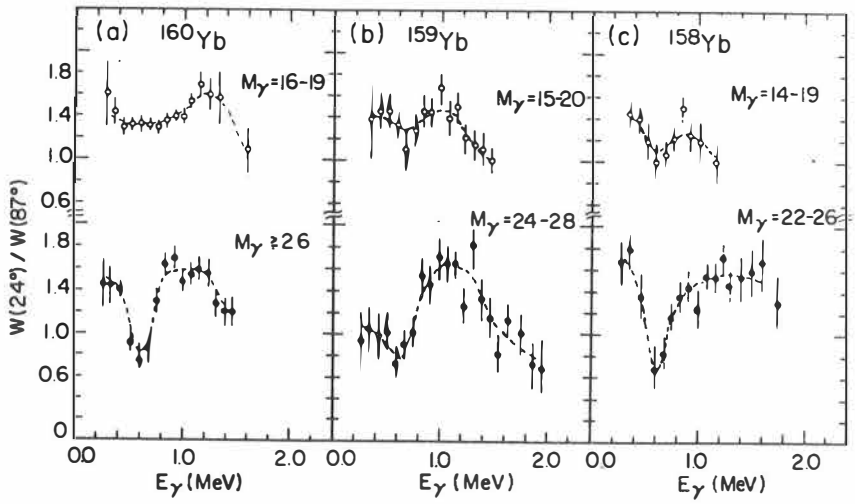

Fig. 32. Anisotropies of the continuum γ-rays in (a) ^{160}Yb, (b) ^{159}Yb and (c) ^{158}Yb for different multiplicity bins as indicated.

dipole in character as seen from the anisotropies for $M \gtrsim 25$ (fig. 32a). This can be seen also from fig. 33 which shows the γ-ray spectra of ^{160}Yb from an NaI detector at 24^{o} and 87^{o} for $M \geq 27$.

The anisotropy information together with difference spectra constructed from successive multiplicities indicates that the dipole to the quadrupole ratio above $M_{\gamma} > 25$ is about one. Again the appearance of the dipole transitions occurs exactly at the same multiplicity where the entry line $\langle E^{*} \rangle$ vs. M (fig. 30) bends down. The constant slope of the entry line above $M \approx 27$ indicates that the ratio of dipole and quadrupole transitions is nearly constant up to the highest multiplicities reached ($M_{\gamma} \approx 32$).

As the neutron number is decreased going to lighter Yb isotopes, the appearance of the dipole component shifts toward lower multiplicities

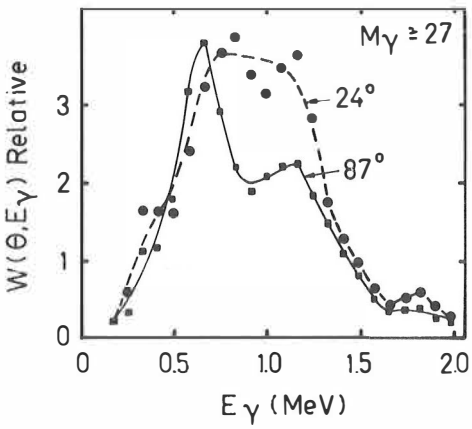

Fig. 33. γ-ray spectra for $M \geq 27$ from the $^{146}Nd(^{20}Ne, 6n)^{160}Yb$ reaction at 149 MeV obtained at $\theta = 24.4^{o}$ and 87.3^{o} relative to the beam direction. The curves are drawn to guide the eye.

as seen from the results in fig. 29 and 30. For ^{159}Yb the onset of the dipoles and the change in the slope of the entry line occur at $M \approx 23$.

The spins associated with each multiplicity in these nuclei were derived with the aid of the statistical model calculations. The rotational picture used in the calculations reproduces the slopes of the entry lines below the onset of the dipole radiation. In this region the average spin for each multiplicity was obtained from the calculated entry states as a function of M and of I using the expression

$$(35) \qquad \langle I \rangle = [\sum_{I} I * S(I, M)] / \sum_{I} S(I, M)$$

where $S(I, M)$ is the calculated distribution connecting I to M. For higher multiplicities the additional stretched $\Delta I = 1$ transitions were accounted for by changing the M to I mapping described above the downbent by a factor of 0.75 corresponding equal numbers of dipole and quadrupole transitions. This procedure gives for the onset of the new

decay mode the value $I \simeq 50$ ($M = 27$), $I = 45$ ($M \approx 25$) and $I = 42$ ($M \approx 23$) in ^{161}Yb, ^{160}Yb and ^{159}Yb, respectively. The presence of dipole transitions also explains the apparently slower evolution of the edge of the quadrupole bump with M because now $\Delta I/\Delta M \approx 1.5$. With correct M to I mapping a smooth dependence of the effective moment of inertia ϑ_{eff} on I is obtained as shown in fig. 34 for ^{160}Yb. The effective moment of inertia was derived from the mid point of the upper edge of the quadrupole bump, assuming rotational behavior. The smooth evolution of ϑ_{eff} with I in the range of $I = 45 - 55$ is completely consistent with collective rotational behavior. The behavior of ϑ_{eff} with spin is close to the predictions of the rotating liquid drop model. However, the absolute value at $I \sim 45$ is somewhat higher and the increase with spin slightly faster than predicted.

In summary the experimental data for ^{159}Yb, ^{160}Yb and ^{161}Yb show a rotational behavior with stretched E2 decay up to spin 42, 45 and 50, respectively. Above that spin a change in the decay mode occurs. This new decay mode has a strong dipole component at $\sim$ 650 keV and a quadrupole component at twice the energy ($\sim$ 1300 keV). This onset of a new decay mode effects also the entry lines $\langle E^* \rangle$ vs. M which have a downbent. However, the effective moment of inertia determined from the edge of the quadrupole bumps evolves smoothly. It should be pointed out that a "super backbend" would result if the effect of the dipoles in M to I mapping is not taken into account.

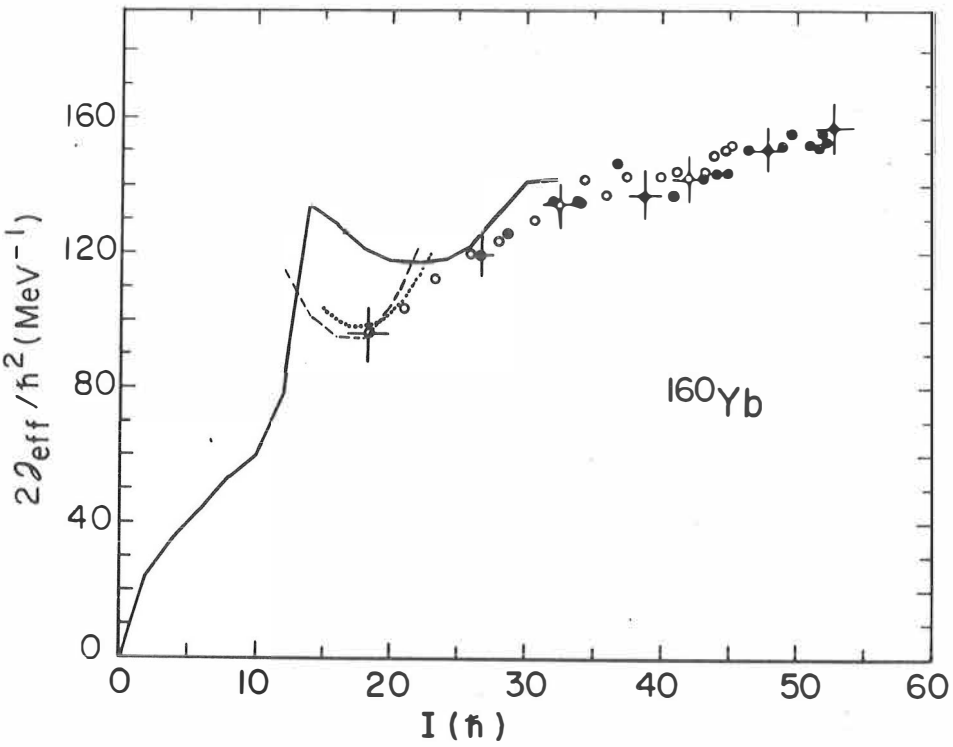

Fig. 34. The effective moment of inertia of ^{160}Yb obtained from the upper edge of the quadrupole γ-ray spectrum. The solid points are for 149 MeV data and the open circles are for 136 MeV data. The solid, dashed and dotted lines at low spin connect points for the yrast and side bands 1 and 2 from discrete line spectroscopy [34].

5.5. Yrast-like transitions in ^{158}Yb and ^{157}Yb

As seen from fig. 30 and 32 the decay of ^{158}Yb has the same overall structure as the heavier isotopes. However, its behavior as a function of spin is even more complicated but also even more interesting.

The observed entry lines <E*> vs. M shown in fig. 30c have four different slopes as a function of multiplicity. The changes of the slopes of the entry lines <E*> vs. M are, again, associated with changes in the γ-ray spectra. Selected energy spectra from the 8n reaction, obtained from all the NaI detectors in the spectrometer and normalized to their respective multiplicities are shown in fig. 35a. They correspond to selected single k values. Spectra from the 6n reaction corresponding to bins of three consecutive k values are shown in fig. 35b. The labels in fig. 35 are then mean values of M corresponding to each k-bin. The sharp edges may be deceptive, as the M gates actually extend about 2 units above and below the indicated ranges due to the finite M resolution of the spectrometer.

The yrast decay scheme of ^{158}Yb is known up to I = 12 and consists of a cascade of stretched E2 transitions, with E_γ from 358 to 683 keV [49]. The behavior of the observed γ-ray spectra is consisted with a continuation of a predominantly quadrupole cascade at least up to M $\approx$ 15. The angular distribution of the γ-rays for M between 14 and 20 are less anisotropic than would be expected for pure quadrupole radiation, as seen from fig. 32c. Moreover at M $\approx$ 16 - 20 the additional contribution to the γ-ray spectra with increasing M occur not only at the E_γ edge but almost equally between 0.5 - 1.0 MeV as seen from fig. 35. This observation suggests a tendency toward non-collective transitions, which in the lighter rare earth nuclei have been associated with aligned quasiparticle structure with small oblate deformation [9]. Recent results from discrete line spectroscopy show a change to single particle structure at I $\approx$ 30 for ^{158}Yb [50]. This observation is in perfect agreement with the continuum data observed in ^{158}Yb.

A different behavior is seen at higher M. Above M $\approx$ 22 the addi-

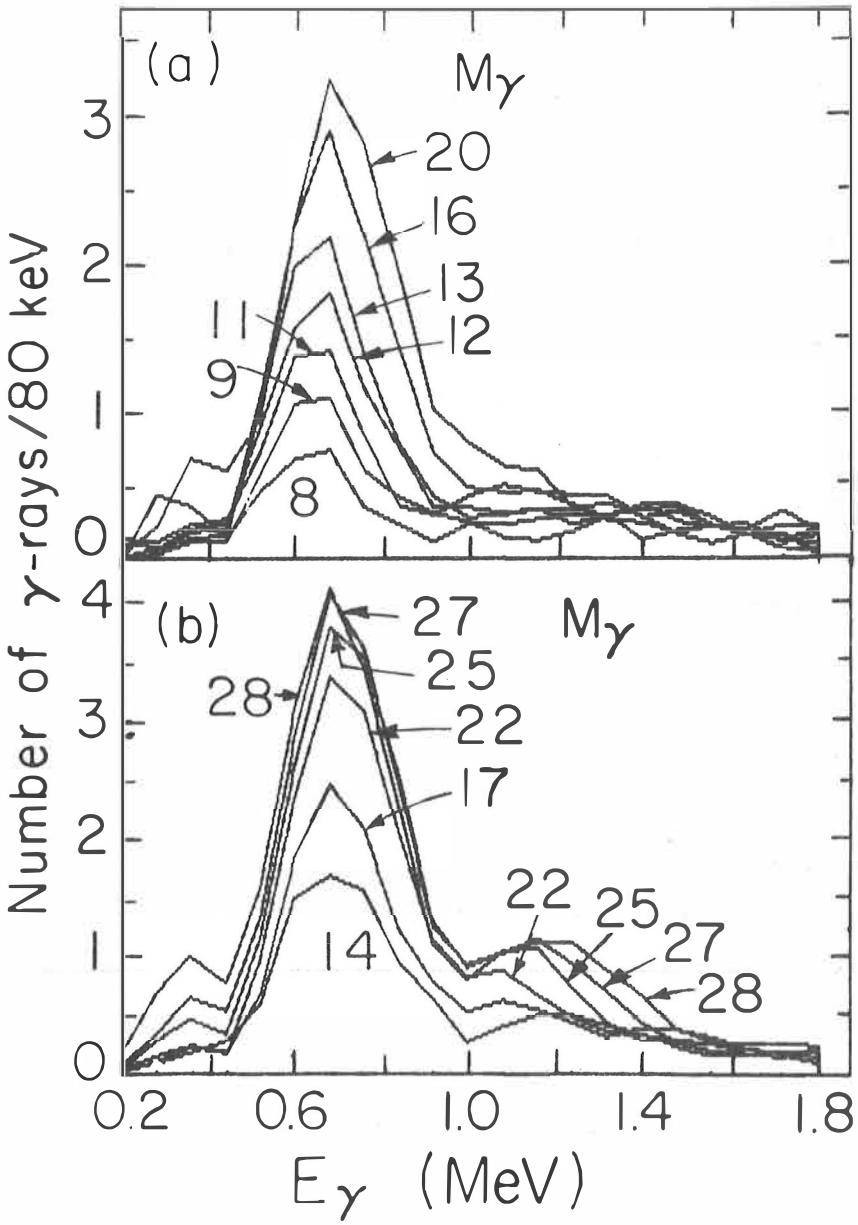

Fig. 35. The continuum γ-rays from the
(a) $^{146}Nd(^{20}Ne, 8n)^{158}Yb$ reaction at 149 MeV
(b) $^{144}Nd(^{20}Ne, 6n)^{158}Yb$ reaction at 149 MeV

tional γ-rays are localized into two separate components and the entry line (fig. 30c) begins to bend down significantly. In the same M region the lower half ($E_\gamma \sim 700$ keV) of the spectrum develops an angular distribution characteristic of stretched dipole radiation as seen from fig. 32c. All three observations are consistent with the onset at $M_\gamma \simeq 22$ of a strong dipole component which is well localized in E_γ. This behavior is exactly the same as observed in $^{159\text{-}161}$Yb at high spin. From the spectra at various angles it can be estimated that the dipole energies are confined to a narrow energy region at ~ 650 keV with a full width half maximum of ~ 200 keV.

For $M \gtrsim 22$ the high energy bump above $E_\gamma = 1200$ keV becomes increasingly prominent. This bump evolves up to the highest M in just the way expected for a rotational quadrupole cascade with approximately constant moment of inertia. The angular distribution data show clearly that the transitions in this energy region are stretched E2.

Another change in decay mode at high M is apparent in fig. 35b. The dipole component at $E_\gamma \sim 650$ keV stops increasing at $M \simeq 27$. This is entirely consistent with the behavior of the entry line (fig. 30) which shows an upbend at this M. Above M = 28 the entry line has resumed the slope expected for predominantly quadrupole cascades.

To summarize the experimental observations, the continuum spectroscopy of ^{158}Yb can be divided into four angular momentum regions with distinctive characteristics. At low spin ($I \lesssim 25$) ^{158}Yb decays like a prolate rotor or that changing slowly toward an oblate shape. At moderate spins ($I \sim 30 - 38$) there is evidence for noncollective effects in the continuum. At $I \simeq 38$ ($M \simeq 22$) a strong stretched dipole component appears at an energy ($E_\gamma \simeq 650$ keV) one half the quadrupole edge at the same spin. These dipoles account for 50 % of the additional transitions

between I = 38 and 48. Nevertheless a stretched quadrupole component continues to evolve over this spin range in the way expected of a rotational spectrum. I ≃ 48 is another transition point. Above this spin no additional stretched dipole transitions were seen.

The γ-ray decay of ^{157}Yb was studied using the ^{144}Nd(^{20}Ne, 7n)^{157}Yb reaction at 149 MeV for the multiplicity range from 8 to 23. For this limited range of M the mean features of the γ-ray decay are identical to that of ^{158}Yb as seen from fig. 29. At low spin a stretched E2 cascade is seen and the aligned single particle character is observed at I ~ 20 - 35 (M ≈ 12 - 18). The onset of the new decay mode characterized by localized dipole and quadrupole transitions occur at I ≈ 36 (M ≈ 20).

5.6. Decay modes in $^{157\text{-}161}$Yb as a function of spin

The observed γ-ray decay modes in $^{157\text{-}161}$Yb as a function of angular momentum have a similar pattern as seen from the data shown in the previous sections. In all the five isotopes from N = 87 to 91 the decay of the low spin states occur via stretched E2 transitions. The lighter isotopes ^{157}Yb and ^{158}Yb have a distinguished single particle structure at I ~ 20 - 36 and I ~ 30 - 38, respectively. Thus at intermediate spins they have the same kind of decay spectrum as lighter rare earth nuclei at A ~ 150 have from low spin up to I ≈ 40 [6]. Even the decay spectra from ^{159}Yb (N = 89) show some signs of the existence of such a region at I ≈ 35 - 40 but the resolution used in these experiments does not allow to confirm this fully. The heavier isotopes, however, do not seem to have any single-particle transitions in the decay of the entry states populated. At I = 36, 38, 42, 45 and 50 in $^{157\text{-}161}$Yb, respectively,

a new completely different decay mode sets in. This decay mode involves dipole transitions localized to $E_\gamma \approx 600 - 700$ keV and simultaneous quadrupole transitions at twice the energy of the dipole transitions. The energy of these transitions in all isotopes is about equal for a given spin above the onset of the new decay mode. The γ-ray decay in the $N \gtrsim 89$ isotopes changes directly but smoothly to this new decay mode from pure stretched E2 cascades as spin increases within a relatively narrow spin range ($\Delta I \sim 4$). In lighter isotopes the new decay mode "grows" on top of a single-particle structure. In addition the dipole transitions disappear at $I \sim 48$ in ^{158}Yb and at the higher spin ($I \gtrsim 50$) it decays via pure $E_\gamma \approx 1400$ keV quadrupole transitions. All these decay modes observed in the γ-ray spectra are also reflected in the slopes of the entry lines $\langle E^* \rangle$ vs. M. It should be noted that if a transition to $\langle E^* \rangle$ vs. I space is done based on the observed quadrupole to dipole ratio a smooth $\langle E^* \rangle$ vs. I entry line is obtained. The effective moments of inertia determined from the upper edge of the spectrum also behave in a reasonable fashion. For the heavier isotopes a smooth behavior close to the liquid drop estimates can be seen through all spin values. The lighter isotopes also show a nice behavior at low spin and above $I \sim 40$. At intermediate spin, where this "rotational definition" of the effective moment of inertia, does not work because of the single-particle character of the decay (edge determined by E2 transitions at $I < 30$). Thus the values at $I \sim 30 - 40$ are too high and there is a discontinuity at the point ($I \sim 40$) where collectivity sets in. This can be seen from fig. 36 which shows the calculated moment of inertia for ^{158}Yb as a function of spin. At low spin the moment of inertia increases faster than for the heavier isotopes mainly because of smaller deformation. At high spin, above the onset of the new decay mode, the moments of

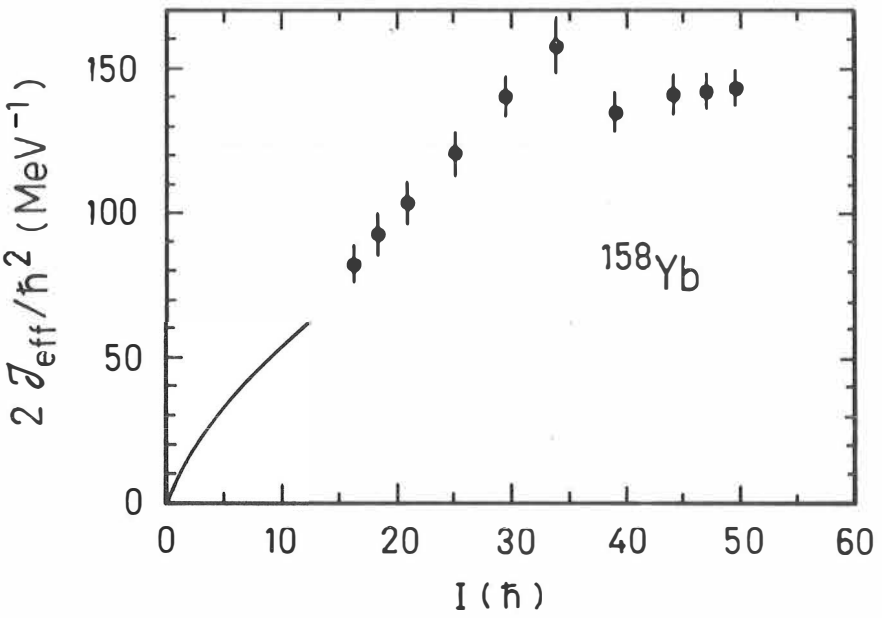

Fig. 36. Effective moment of inertia as a function of spin for ^{158}Yb. The effective moment of inertia was defined as described in text.

inertia of all isotopes are the same. This indicates that the structure of all isotopes is very similar at high spin although their behavior at low spin differs. Recently an exactly the same decay mode with localized dipoles and quadrupoles has been found at high spin ($I > 40$) in ^{152}Dy [51] which has an oblate single-particle structure at lower spin [6].

6. EVOLUTION OF THE NUCLEAR STRUCTURE AS A FUNCTION OF SPIN AND NEUTRON NUMBER

The evolution of the nuclear structure as a function of angular momentum and proton or neutron mumber is of fundamental importance in understanding the interplay of the collective and single-particle degrees of freedom which determines the behavior of nuclei away from closed shells. Experimentally only a few nuclei have been found to obtain an oblate ground state. With increasing angular momentum, however, an alignment of quasiparticle angular momenta tends to make the nucleus oblate.

The nuclei around $A \sim 150$ are knwon to have few-particle yrast states up to $I \approx 38$ with small oblate deformations ($\varepsilon \sim 0.1 - 0.2$) [52]. This behavior is well understood also with the rotating liquid drop model [39]. It predicts the spherical nucleus at $I = 0$ to deform and increase its moment of inertia by flattening at poles when angular momentum is increased. This oblate nucleus can increase the moment of inertia further by breaking the axial symmetry. For nuclei around $A = 160$ this occurs at $I \approx 70$ followed by a fast deformation leading to fission with increasing angular momentum. This simplified picture of the behavior of the nucleus with angular momentum is strongly modified by the underlying nuclear shell structure.

At low spin up to $I \approx 15 - 20$ the pairing affects the nucleus significantly and the nuclei with $N \geq 92$ obtain a prolate shape with 20 - 30 % deformation [53]. In these nuclei the excitation energy and angular momentum is gained via collective rotation around an axis perpendicular to the symmetry axis. As the rotational frequency increases the classical

Coriolis force causes alignment of a few individual particle angular momenta along the collective angular momentum [54]. These changes can break the axial symmetry of the nucleus but the basic structure is still close to a prolate shape ($\gamma \approx 0^{o}$). A massive alignment of individual quasiparticle angular momenta along the spin axis and the rotation can increase the shell energy for a prolate shape and can finally change the nucleus to a basically oblate shape ($\gamma \approx 60^{o}$) [55]. In this nucleus the angular momentum is mainly formed by the sum of individual quasiparticle angular momenta. Thus the tendency for prolate nuclei to become oblate with increasing angular momentum is a combined liquid drop and shell effect. The rotational frequency required to align quasiparticles is proportional to the strength of the pairing. Thus the lighter Yb isotopes with smaller prolate deformation at the ground state can align their quasiparticle angular momenta at lower spin.

For nuclei with $N > 90$ the negative shell energy for prolate shape is so strong that a transition from prolate to oblate shape is not likely [55]. Thus the nuclei with $N = 88 - 90$ on the border of the deformation region are the most probable candidates for such a change. Once large amounts of particle orbits are aligned and thus a large oblate deformation obtained, the nucleus can be additionally excited via collective motion.

The shell structure effects still existing at high angular momenta are expected to cause some nuclei to break the oblate axial symmetry at lower spin than expected from the rotating liquid drop model. This can lead to a fast increase in deformation with increasing spin and to a rapid growth of the moment of inertia and finally to the "superdeformed triaxial" nucleus [56,57].

6.1. Nuclear shape changes

Detailed systematic calculations for the nuclear structure of the Yb isotopes, based on a cranked modified-oscillator shell model, have recently been performed at the University of Lund [10,58,59]. The results for the equilibrium shapes as a function of angular momentum from their calculations, combined with known pairing effects, are shown for $^{157\text{-}161}$Yb with the solid line in fig. 37. These calculations can be used as a frame

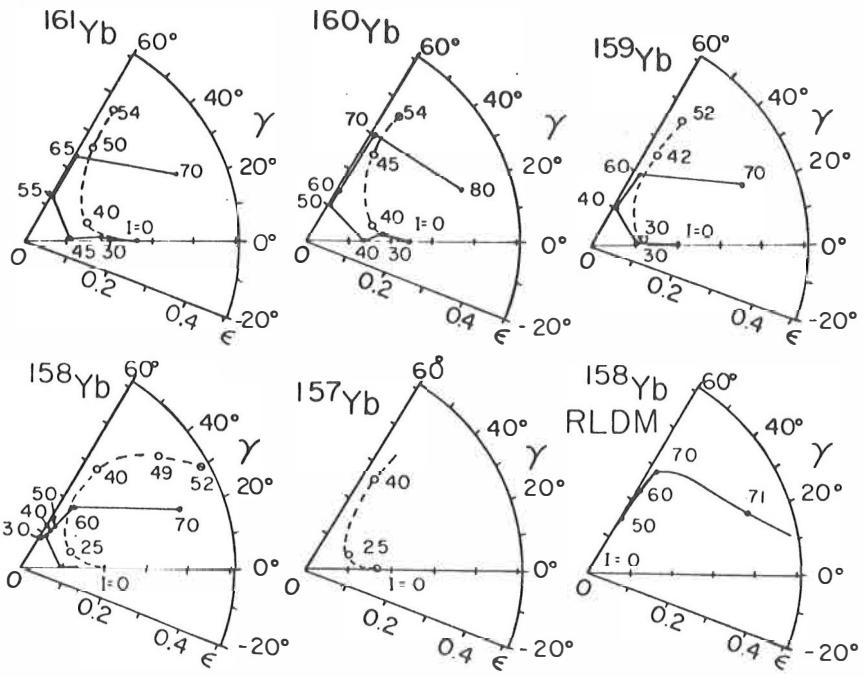

Fig. 37. Trajectories of equilibrium shapes in (ε , γ) plane for N = 91 - 87 Yb isotopes. The solid lines are from the calculations in ref. 59. The dashed lines represent pictorically the shapes interpreted from the data using the model described in Sect. 6.2. The model described in Sect. 6.3. approximately reproduces the calculations. The last figure shows the shapes obtained with rotating liquid drop model (RLDM) for comparision (^{158}Yb only).

for a possible interpretation of the changes in the decay modes observed in $^{157\text{-}161}$Yb. Near the ground state all the Yb isotopes should be prolate due to the effects of pairing. At higher spins a systematic decrease in deformation along the prolate axis ($\gamma \approx 0$) is predicted. As angular momentum further increases, a sudden change to oblate shape is predicted for the lighter Yb isotopes. The occurrence of the shape change moves smoothly to higher spins as neutron number is increased. At even higher spins, evolution back toward the prolate shape is predicted to occur via an intermediate triaxial configuration. Thus ^{160}Yb is predicted to change to oblate shape between I = 40 and 50 and to remain oblate up to I = 70, whereas ^{158}Yb is predicted to change to oblate shape at lower spins and then become triaxial above $I \approx 50$.

The observed γ-ray decay spectra for ^{157}Yb and ^{158}Yb at $I < 40$ suggest a behavior such as that seen in the N = 88 nucleus ^{154}Dy [60] with a rotational behavior at the lower spins followed by the onset of an irregular behavior characteristic of a particle aligned oblate structure ($\varepsilon \approx 0.15$) like seen in ^{152}Dy [6]. Recent study of the discrete lines in ^{158}Yb up to $I \approx 34$ [50] confirm fully this behavior observed in the continuum data. The transition to single-particle structure was seen at $I \approx 30$, exactly at the spin value interpreted from the continuum data. This region of quasiparticle structure extends up to $I \approx 40$. In ^{157}Yb the transition to oblate shape occur at $I \approx 20$ and the single-particle structure seems to dominate up to $I \approx 38$.

6.2. High K-bands

The observation of the single-particle structure and the results of the shell model calculations would indicate that the new decay mode with localized dipoles and quadrupoles is associated with oblate shape. This can be seen from fig. 38 where the regions of different nuclear shapes obtained from the calculations (combined with the information from

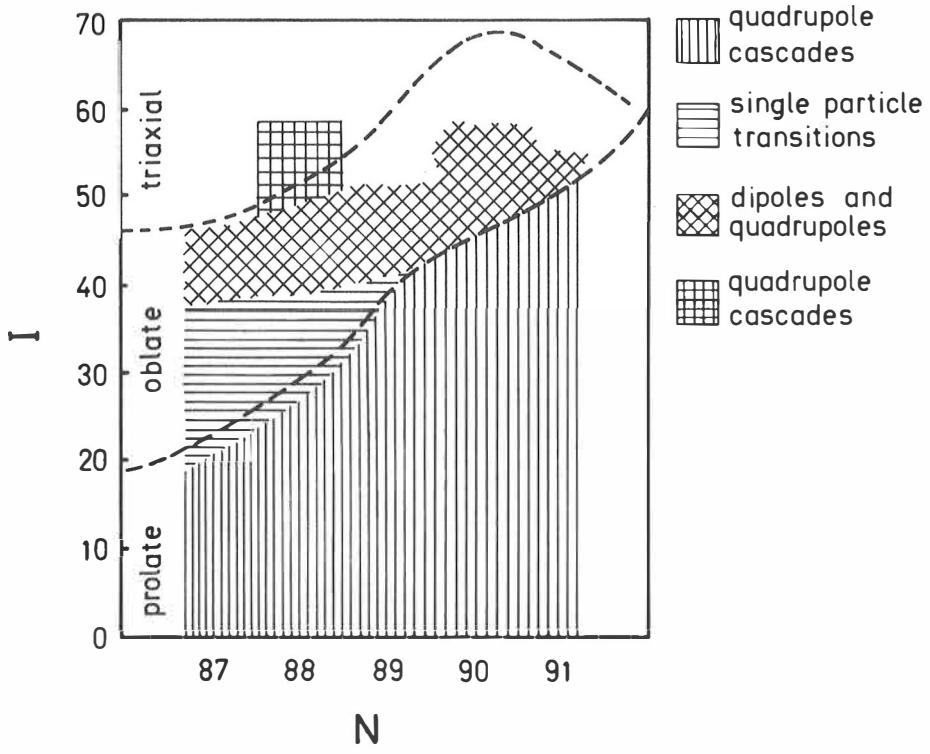

Fig. 38. Regions of different nuclear shapes of N = 87 - 91 Yb isotopes obtained from the calculations in ref. 59 compared to different decay modes observed in the experimental data.

discrete line spectroscopy) are compared with the observed regions of different γ-ray decay modes. As seen the oblate shape coincides completely with the region of sp transitions and the new decay mode. The strong localization of the dipole transitions near half the energy of the quadrupole transitions observed at the same multiplicities, it is obvious that transitions in collective bands are responsible for these γ-rays. The yrast states of an oblate nucleus, whatever their deformation is, are most likely to be aligned quasiparticle states with spin vector along the symmetry axis. Thus these states are high K states ($K \approx I$) upon which if the deformation is sufficient collective states could be built on. The decay of such states in the high-K bands is expected to include strong intraband M1 transitions [58,61] because in the rotational model $B(M1) \propto K^2$ while $B(E2) \propto 1/K$. Thus the dipoles would dominate near the band heads and if the decay occurs through a series of such bands lying close to the yrast line a proper M1/E2 ratio could be reached. The remarkable location of dipole radiation at half the quadrupole energies supports this intraband M1 speculation assuming that these bands lie parallel to the yrast line. For $2\,\vartheta_{eff}/\hbar^2 = 150\ MeV^{-1}$ and $I = 45$ the dipole component should occur at 640 keV [61] in agreement with the observation [61]. Furthermore the smooth behavior of the effective moment of inertia at $I > 40$ in these nuclei agrees with the "oblate rotor" picture. The M1 peak should also move to higher energy with increasing spin as the E2 transitions do. However, the total shift from $I = 40$ to 50 should be only about 100 keV and thus this possibility is not ruled out although it is not seen in the data. Even finer entry selection would be needed to confirm this.

In order to have collective rotational bands built on the high-K single-particle states a fairly large deformation is needed [61,62].

Recent theoretical RPA calculations of the wobbling motion for ^{158}Yb [63] show that a deformation of $\varepsilon \gtrsim 0.25$ is required in order to reproduce the energy of the dipole radiation in the K range from 40 to 50.

For the isotopes $A \geq 159$ it appears that the transition to the oblate shape occurs with deformation large enough to allow collective motion. The systematic evolution of the decay modes as a function of spin and neutron number in N = 87 - 91 Yb isotopes observed in the experiment correlates well with the calculated evolution of the nuclear shapes in these nuclei. The evolution of the shape change with neutron number can also be understood from the simple shell model picture. As the prolate deformation of the lighter isotopes is smaller it is easier to align the particles as the rotational frequency increases. Thus they align particles at lower spins. This is seen as an intense quadrupole bump at 600 - 800 keV at low spin instead of a steady growth of the maximum energy as in the heavier isotopes. This faster alignment also leads to an oblate shape at lower spins. The change occurs at $I \cong 20$, 30, 40, 45 and 50 for $^{157-161}$Yb respectively. The data from later experiments [64] show that no change is seen in ^{162}Yb up to the highest spin ($I \sim 60$) reached with the ^{50}Ti + Sn reaction at 250 MeV. This also is in agreement with the shell model calculations. The onset of a new decay mode with localized dipoles and quadrupoles occurs at I = 38, 40, 42, 45 and 50 for $^{157-161}$Yb respectively. This decay mode most possibly associated with collective oblate states occurs only above spin $\sim 40\ \hbar$. This could indicate that a larger deformation is needed. For the heavier isotopes the deformation is sufficient so that the change occurs directly to the collective states. However, the lighter isotopes do not have enough deformation at the spin where the shape change occurs. Thus they have a spin range with single-particle states.

6.3. Oblate state terminating bands

The high-K band interpretation of the observed γ-ray decay requires quite large oblate deformation in order to produce the localization of the dipole radiation. This value ($\varepsilon \sim 0.25$) is somewhat larger than expected for the aligned single particle states at $I \sim 40$ for rare earth nuclei ($\varepsilon \sim 0.15$) [55]. However, the full understanding of the nature of these bands requires further experimental and theoretical study [52]. Especially the effects of the core polarization as a result of large alignment and the behavior of these bands with excitation above the yrast line are of great importance. Another possible explanation is that the observed dipole and quadrupole components are the terminating bands of cranked Nilsson-Strutinsky formalism [65]. According to recent calculations by Bengtsson and Ragnarsson [65] M1-transitions are favored near the band terminations for the configurations which terminate to an oblate aligned state. This model is basicly the same as that used to explain the rotational bands in ^{20}Ne [66] at low spin, but applied to the rare earth region. In ^{20}Ne the highest member of the band corresponds to an alignment of the angular momenta of all the particles outside closed shells and is therefore an oblate state where the nucleus is rotating around the symmetry axis ($K = I$). For such a rotational motion, the E2 transition probability vanishes [67]. In the $A \sim 160$ region there are more particles outside the core and thus these band terminations appear at high spin. Also the number of possible configurations is much greater. The new application to $A \sim 160$ requires thus that the calculations follow individual configurations as a function of spin and the terminating state of these bands is the highest spin which can be formed with the given distribution of particles over the j-shell. The calcula-

tions in ref. 65 were done for ^{158}Er but the results can be applied to the nuclei around A = 160. The lowest oblate configuration that becomes yrast is $\pi(h_{11/2})^4_{16}\ \nu[(f_{7/2})^3(h_{9/2})^3(i_{13/2})^2]_{30}$. The highest member of this configuration is I = 46. This would perfectly fit to the observation of the onset of the dipoles at I $\sim$ 45 in ^{160Y}b. Interestingly the energies of the M1-transitions in these bands at I $\sim$ 40 - 50 are $\sim$ 650 keV [65]. The ε-deformation obtained from these calculations is considerably lower ($\varepsilon \sim 0.12$) than would be required for the high-K band interpretation to explain the observed γ-ray energies. If the observed data and the calculations of ref. 65 are combined, the schematic pathways of the equilibrium shapes from the calculations of ref. 48 (fig. 38) can be qualitatively reproduced.

7. SUMMARY

The Spin Spectrometer was designed to be used in the investigation of nuclear structure at high spin and of heavy-ion induced reactions. The first experiments were performed with minimal auxliar configuration using only one Ge detector. However, the results of these experiments reported in this thesis demonstrate the power of the instrument. The main advantage of a 4π multidetector system over any previous instrument or method is the capability to measure both the γ-ray multiplicity and the excitation energy simultaneously with high accuracy for each event. Thus for the first time the angular momentum (or spin) dependence of various parameters can be determined directly. Furthermore, the high efficiency of the spectrometer enables the selection of the exit channels in addition to the characteristic parameters. This is absolutely necessary in the study of fusion like reactions and the properties of **nuclei.**

The unique information available from the spectrometer also requires complex calibration and data-analysis methods. The use of this instrument as an efficient filter to enhance eg. high multiplicity events is tempting and sometimes also very useful. However, the spectrometer is even more powerful and can provide more information. That is why the response of the instrument was studied in a great detail during the construction and the data-analysis of the first experiments. The results of this pioneer work were reported in Chapter 2. The new calibration methods developed for the spectrometer can be useful also for the development of similar instruments and the study of the responses has already been of great value for different experiments utilizing the spectrometer.

The entry state populations in heavy-ion induced fusion reactions has been discussed since these reactions became tools in high spin spectroscopy, but no direct measurements of the multiplicity distributions or even the

entry lines have been obtained. Thus the entry state populations discussed in Chapter 4 are long awaited. The comparison with statistical-model calculations shows that the fusion reactions can be described with the statistical-model but the measured diffuseness is smaller than expected. The results also indicate that the strenght of the giant dipole resonance is important in the decay of highly excited nuclei at high angular momentum.

For the first time a systematic study of the continuum yrast-like γ-rays in the transitional rare earth nuclei with exit channel selection was done. The increased selectivity has produced results which could not be obtained with any previous methods. The transition from collective (prolate) states at low spin to a region of single particle (oblate) structure in ^{157}Yb and ^{158}Yb at $I \approx 20$ and 30, respectively, is a good indication about the largely discussed shape change of nuclei with increasing angular momentum. These results obtained with continuum studies were excatly confirmed afterwards using the discrete line spectroscopy [50].

The new decay mode with dipole transitions at 600-700 keV and a quadrupole component at twice the energy observed in $^{157\text{-}161}$Yb at high spin is characteristic for these transitional nuclei. Similar new observations in ^{152}Dy [51] are in full agreement with the association of this decay mode with oblate nuclear shape. Although the connection between the observed data and either of the theoretical explanations (high-K or oblate state terminating bands) discussed in this thesis is not direct, the spin and neutron number dependence of the predictions and observations is remarkable good.

The observation of a systematic shape change as a function of the spin and the neutron number in N = 87-91 Yb isotopes is important in understanding the interplay between the collective and the single particle degrees of freedom in nuclei. This demonstrates that the shape of the nucleus depends not only on the number of nucleons but on the angular momentum as well. To fully understand the behaviour of the nuclei as a function of angular momentum further studies both theoretical and experimental are needed.

Angles of the NaI detectors in the spectrometer.

Detector Number	Position	Centroid θ	Centroid φ	Midpoint θ	Midpoint φ
0	A0	0.00	0.00	0.00	0.00
1	A1	24.42	13.11	24.70	13.11
2	A2	24.42	85.11	24.70	85.11
3	A3	24.42	157.11	24.70	157.11
4	A4	24.42	-130.89	24.70	-130.89
5	A5	24.42	-58.89	24.70	-58.89
6	B0	63.43	180.00	63.43	180.00
7	B1	87.30	-174.61	87.58	-174.56
8	B2	67.93	-153.61	68.01	-153.32
9	B3	41.59	-165.98	41.36	-165.76
10	B4	49.51	155.73	49.38	155.41
11	B5	77.52	158.74	77.69	158.52
12	C0	63.43	108.00	63.43	108.00
13	C1	87.30	113.39	87.58	113.44
14	C2	67.93	134.39	68.01	134.68
15	C3	41.59	122.02	41.36	122.24
16	C4	49.51	83.73	49.38	83.41
17	C5	77.52	86.74	77.69	86.52
18	D0	63.43	36.00	63.43	36.00
19	D1	87.30	41.39	87.58	41.44
20	D2	67.93	62.39	68.01	62.68
21	D3	41.59	50.02	41.36	50.24
22	D4	49.51	11.73	49.38	11.41
23	D5	77.52	14.74	77.69	14.52
24	E0	63.43	-36.00	63.43	-36.00
25	E1	87.30	-30.61	87.58	-30.56
26	E2	67.93	-9.61	68.01	-9.32
27	E3	41.59	-21.98	41.36	-21.76
28	E4	49.51	-60.27	49.38	-60.59
29	E5	77.52	-57.26	77.69	-57.48
30	F0	63.43	-108.00	63.43	-108.00
31	F1	87.30	-102.61	87.58	-102.56
32	F2	67.93	-81.61	68.01	-81.32
33	F3	41.59	-93.98	41.36	-93.76
34	F4	49.51	-132.27	49.38	-132.59
35	F5	77.52	-129.26	77.69	-129.48
36	G0	180.00	180.00	180.00	180.00
37	G1	155.58	166.89	155.30	166.89
38	G2	155.58	94.89	155.30	94.89
39	G3	155.58	22.89	155.30	22.89
40	G4	155.58	-49.11	155.30	-49.11
41	G5	155.58	-121.11	155.30	-121.11
42	H0	116.57	0.00	116.57	0.00
43	H1	92.70	-5.39	92.42	-5.44
44	H2	112.07	-26.39	111.99	-26.68
45	H3	138.41	-14.02	138.64	-14.24
46	H4	130.49	24.27	130.62	24.59
47	H5	102.48	21.26	102.31	21.48
48	I0	116.57	72.00	116.57	72.00
49	I1	92.70	66.61	92.42	66.56
50	I2	112.07	45.61	111.99	45.32

Detector Number	Position	Centroid θ	Centroid φ	Midpoint θ	Midpoint φ
51	I3	138.41	57.98	138.64	57.76
52	I4	130.49	96.27	130.62	96.59
53	I5	102.48	93.26	102.31	93.48
54	J0	116.57	144.00	116.57	144.00
55	J1	92.70	138.61	92.42	138.56
56	J2	112.07	117.61	111.99	117.32
57	J3	138.41	129.98	138.64	129.76
58	J4	130.49	168.27	130.62	168.59
59	J5	102.48	165.26	102.31	165.48
60	K0	116.57	-144.00	116.57	-144.00
61	K1	92.70	-149.39	92.42	-149.44
62	K2	112.07	-170.39	111.99	-170.68
63	K3	138.41	-158.02	138.64	-158.24
64	K4	130.49	-119.73	130.62	-119.41
65	K5	102.48	-122.74	102.31	-122.52
66	L0	116.57	-72.00	116.57	-72.00
67	L1	92.70	-77.39	92.42	-77.44
68	L2	112.07	-98.39	111.99	-98.68
69	L3	138.41	-86.02	138.64	-86.24
70	L4	130.49	-47.73	130.62	-47.41
71	L5	102.48	-50.74	102.31	-50.52

The angles θ and ϕ in the table are the polar and azimutal angles in a spherical polar cordinate system for which the outgoing beam defines the polar axis and upward vertical direction is taken as $\phi = 0$. The angles $\phi > 180^{\circ}$ have been replaced by $\phi - 360^{\circ}$. Because of the irregularity of the hexagonal detectors there are several ways to define center points on there front faces. The two listed in the table are the centroid of the detector face and the midpoint, which is the center of the largest cyclindrical external detector that can be inserted in the spectrometer in place of a hexagonal element. For the pentagonal detectors these two centers coincide.

REFERENCES

[1] M. Goldhaber and A.W. Sunyar, Phys. Rev. 83 (1951) 906

[2] F. Asaro and I. Perlman, Phys. Rev. 91 (1953) 763

[3] T. Huus and C. Zupancic, Mat. Fys. Medd. Dan. Vid. Selsk. 1 (1953) 28

[4] H. Morinaga and P.C. Gugelot, Nucl. Phys. 46 (1963) 210

[5] F.S. Stephens, D. Ward and J.O. Newton, Jpn. J. Phys. Suppl. 24 (1968) 160

[6] T.L. Khoo, R.K. Smither, B. Haas, O. Häusser, H.R. Andrews, D. Horn and D. Ward, Phys. Rev. Lett. 41 (1978) 1027

[7] J. Burde, E.L. Dines, S. Shih, R.M. Diamond, J.E. Draper, K.H. Lindenburger, C. Schuck and F.S. Stephens, Phys. Rev. Lett. 48 (1982) 530

[8] R.M. Diamond and F.S. Stephens, Ann. Rev. Nucl. Part. Sci. 30 (1980) 85

[9] A. Bohr and B.R. Mottelson, Phys. Scripta 10A (1974) 13

[10] R. Bengtsson, S.E. Larsson, G. Leander, P. Moeller, S.G. Nilsson, S. Åberg and Z. Szymanski, Phys. Lett. 57B (1975) 301

[11] G.B. Hagemann, R. Broda, B. Herskind, M. Ishihara, S. Ogaza and H. Ryde, Nucl. Phys. A245 (1975) 155

[12] D.G. Sarantites, J.H. Barker, M.L. Halbert, D.C. Hensley, R.A. Dayras, E. Eichler, N.R. Johnson and S. Gronemeyer, Phys. Rev. C 14 (1976) 2138

[13] L. Westerberg, D.G. Sarantites, R. Lovett, J.T. Hood, J.H. Barker, C.M. Currie and N. Mullani, Nucl. Instr. and Meth. 145 (1977) 295

[14] P.O. Tjøm, F.S. Stephens, R.M. Diamond, J. deBoer and W.M. Meyerhof, Phys. Rev. Lett. 33 (1974) 593

[15] R. Albrecht, W. Dunnweber, G. Graw, H. Ho, S.G. Steadman and J.P. Wurm, Phys. Rev. Lett. 34 (1975) 1400

[16] J.B. Natowitz, M.N. Namboodiri, P. Kasiraj, R. Eggers, L. Adler, P. Gonthier, C. Cerruti and T. Alleman, Phys. Rev. Lett. 40 (1978) 751

[17] A. Kerek, J. Kihlgren, Th. Lindblad, C. Pomar, J. Sztarkier, W. Walus, O. Skeppstedt, J. Bialkowiski, J. Kownacki, Z. Sujkowski and A. Zglinski, Nucl. Instr. and Meth. 150 (1978) 483

[18] P.R. Christensen, F. Folkman, Ole Hansen, O. Nathan, N. Trautner, F. Videbaek, S.Y. van der Werf, H.C. Britt, R.P. Chestnut, H. Freiesleben and F. Pühlhofer, Phys. Rev. Lett. 40 (1978) 1245

[19] W.J. Ockels, M.J.A. de Voigt and Z. Sujkowski, Phys. Lett. 78B (1978) 401

[20] D.G. Sarantites, L. Westerberg, M.L. Halbert, R.A. Dayras, D.C. Hensley and J.H. Barker, Phys. Rev. C 18 (1978) 774

[21] L. Westerberg, D.G. Sarantites, D.C. Hensley, R.A. Dayras, M.L. Halbert and J.H. Barker, Phys. Rev. C 18 (1978) 796

[22] K.A. Geoffroy, D.G. Sarantites, M.L. Halbert, D.C. Hensley, R.A. Dayras and J.H. Barker, Phys. Rev. Lett. 43 (1979) 1303

[23] F. Folkmann, J.D. Garrett, G.B. Hagemann, M.N. Harakeh, B. Herskind, D.L. Hillis, S. Ogaza, H. Emling, E. Grosse, D. Schwalm, R.S. Simon and P.O. Tjøm, Nucl. Phys. A361 (1981) 242

[24] P. Chowdhury, J. Borggreen, T.L. Khoo, I. Ahmad, R.K. Smither, S.R. Faber, P.J. Daley, C.L. Dors and J. Wilson, Phys. Rev. Lett. 47 (1981) 778

[25] D.G. Sarantites, R. Lovett and R. Woodward, Nucl. Instr. and Meth. 171 (1980) 503

[26] Harshaw Chemical Co., Solon, Ohio.

[27] D.C. Hensley, IEEE Transactions on Nuclear Science, Vol. NS-28, No. 5, p. 3720 (1981)

[28] LeCroy Research Corp. Model 612A 12-channel linear amplifiers

[29] LeCroy Research Corp. Model 2249W, 12-Channel A-to-D Converter

[30] LeCroy Research Corp. Model 2228A Octal Time-to-Digital Converter

[31] A larger version of the device described by D.C. Hensley IEEE Transactions on Nuclear Science, Vol. NS-26, No. 4, p. 4454 (1979)

[32] LeCroy Research Corp. No. HV4032A 32-Channel High Voltage Supply and Model 2132 CAMAC Interface

[33] D.G. Sarantites, M. Jääskeläinen, J.T. Hood, R. Woodward, J.H. Barker, D.C. Hensley, M.L. Halbert and Y.D. Chan, Journal de Physique 41 (1980) C10

[34] L.L. Riedinger, Nucl. Phys. A347 (1980) 141

[35] J.R. Gover and J. Gilat, Phys. Rev. 157 (1967) 802, 814

[36] D.G. Sarantites and E.J. Hoffman, Nucl. Phys. A180 (1972) 177

[37] J.J. Simpson, P.O. Tjøm, I. Espe, G.B. Hagemann, B. Herskind and M. Neiman, Nucl. Phys. A287 (1977) 362

[38] P.O. Tjøm, I. Espe, G.B. Hagemann, B. Herskind and D.L. Hillis, Phys. Rev. Lett. 72B (1978) 439

[39] S. Cohen, F. Plasil and W.S. Swiatecki, Ann. Phys. (NY) 82 (1974) 55

[40] J. Wilczynski, Nucl. Phys. A216 (1973) 386
J. Wilczynski, K. Siwek-Wilczynsa, J. van Driel, S. Gonggrijp, D.C.J.M. Hagemann, R.V.F. Janssens, J. Lukasiak and R.H. Siemssen, Phys. Rev. Lett. 45 (1980) 606

[41] R. Bass, Nucl. Phys. A231 (1974) 45; Phys. Rev. Lett. 39 (1977) 265

[42] M. Hillman and Y. Eyal, Code JULIAN (unpublished);
A. Gauron, modification PACE, Phys. Rev. C 21 (1980) 230

[43] J.H. Barker and D.G. Sarantites, Phys. Rev. C 9 (1974) 607

[44] J.O. Newton, B. Herskind, R.M. Diamond, E.L. Dines, J.E. Draper and K.H. Lindenberger, Phys. Rev. Lett. 46 (1981) 1383

[45] G.A. Bartholomew et al.
Advances in nuclear physics, eds. M. Baranger and E. Vogt, Vol. 7 (1973) p. 229

[46] S.S. Hana, in: Giant multipole resonances, ed. F. Bertrand (Harwood, New York, 1980) Table I

[47] A. Bohr and B.R. Mottelson, Nuclear Structure, Vol. II (Benjamin, Reading MA, 1975) p. 474ff

[48] A. Bohr and B.R. Mottelson, Phys. Scripta 24 (1981) 71

[49] W. Troutman, D. Proetel, O. Häusser, W. Hering and F. Riess, Phys. Rev. Lett. 35 (1975) 1694

[50] C. Baktash, private communication

[51] D. Ward, H.R. Andrews, B. Haas, P. Taras and N. Rud, Nucl. Phys. A397 (1983) 161

[52] T.L. Khoo, Journal de Physique C 10 (1980) 9

[53] M.A. Deleplanque, J.P. Husson, N. Perrin, F.S. Stephens, G. Bastin, C. Schück, T.P. Thibaud, L. Hildingsson, S. Hjort, A. Johnson and Th. Lindblad, Phys. Rev. Lett. 43 (1978) 100

[54] R. Bengtsson and S. Frauendorf, Nucl. Phys. A327 (1979) 139

[55] I. Ragnarsson, T. Bengtsson, G. Leander and S. Åberg, Nucl. Phys. A347 (1980) 287

[56] T. Bengtsson, M.E. Faber, G. Leander, P. Möller, M. Ploszajczak, I. Ragnarsson and S. Åberg, Phys. Scripta 24 (1981) 200

[57] S. Åberg, S.E. Larsson, P. Möllerr, S.G. Nilsson, G. Leander and I. Ragnarsson, Phys. and Chem. of Fission 1979, Vol. 1 (1980) 303

[58] G. Andersson, S.E. Larsson, G. Leander, P. Möller, S.G. Nilsson, I. Ragnarsson, S. Åberg, R. Bengtsson, J. Dubek, B. Nerlo-Pomorska, K. Pomorski and Z. Szymanski, Nucl. Phys. A268 (1976) 205

[59] S. Åberg, Phys. Scripta 25 (1982) 23

[60] A. Pakkanen, Y.H. Chung, P.J. Daly, S.K. Faber, H. Helppi, J. Wilson, P. Chowdhury, T.L. Khoo, I. Ahmad, J. Borggreen, Z.W. Grabowski and D.C. Radford, Phys. Rev. Lett. 48 (1982) 1530

[61] L.K. Beker, J.H. Hamilton and J.O. Rasmussen, Phys. Rev. Lett. 41 (1978) 152

[62] C.G. Andersson and G. Leander, Nordic Conference on Nuclear Physics, Lysekil, Sweden 1979

[63] P. Arve, Y.S. Chen and G. Leander, Phys. Scripta (in press)

[64] D.G. Sarantites, F.A. Dilmanian, M. Jääskeläinen, H. Puchta, R. Woodward, J.R. Beene, J.H. Barker, M.L. Halbert, J. Hattula, D.C. Hensley, I.Y. Lee, W.T. Milner, F. Plasil, J.J. Gardhøje, J.D. Garrett, G.B. Hagemann, B. Herskind, P. Nolan, G. Stetten and Th. Lindblad, Proc. of Conf. on High Angular Momentum Properties of Nuclei, Oak Ridge TN, 1982 (in press)

[65] T. Bengtsson and I. Ragnarsson, Phys. Scripta (in press)

[66] J.A. Kuehner and E. Almqvist, Can. J. Phys. 45 (1967) 1605

[67] A. Bohr and B.R. Mottelson, Nuclear Structure, Vol. II (Benjamin, Reading MA, 1975) p. 96